Article:
Zhang, Y, Yang, T, Hohl, SV et al. (6 more authors) (2020) Seawater carbon and strontium isotope variations through the late Ediacaran to late Cambrian in the Tarim Basin. Precambrian Research. 105769. p. 105769. ISSN 0301-9268

https://doi.org/10.1016/j.precamres.2020.105769

Seawater carbon and strontium isotope variations through the late Ediacaran to late Cambrian in the Tarim Basin

Yinggang Zhang[1], Tao Yang[1*], Simon V. Hohl[2*], Bi Zhu[3], Tianchen He[4,5], Wenqing Pan[6], Yongquan Chen[6], Xizhu Yao[1], Shaoyong Jiang[1,7]

[1]State Key Laboratory for Mineral Deposits Research, Nanjing University, Nanjing, PR China;

[2]State Key Laboratory of Marine Geology, School of Ocean and Earth Science, Tongji University, Shanghai, PR China;

[3]School of Earth Sciences and Engineering, Hohai University, Nanjing, PR China;

[4]School of Earth and Environment, University of Leeds, Leeds, UK;

[5]State Key Laboratory of Palaeobiology and Stratigraphy & Center for Excellence in Life and Paleoenvironment, Nanjing Institute of Geology and Palaeontology, Chinese Academy of Sciences, Nanjing, PR China;

[6]Research Institute of Exploration and Development, Tarim Oil Field Company, PetroChina, Korla, PR China;

[7]State Key Laboratory of Geological Processes and Mineral Resources, School of Earth Resources, China University of Geosciences, Wuhan, PR China;

*** Corresponding authors: Tao Yang and Simon V. Hohl**

Emails: yangtao@nju.edu.cn and sv_hohl@tongji.edu.cn

Postal address: Nanjing University Xianlin Campus, No.163 Xianlin Avenue, Qixia District, Nanjing, 210046, PR China.

2nd Revised version for submission to Precambrian Research April 2020

Abstract

The radiation of early animals during the Cambrian explosion was accompanied by widespread perturbations in oceanic and atmospheric conditions. However, the cause-effect relationships between evolutionary innovations, carbon (C) cycling, and continental weathering are still a matter of debate. Further paleoenvironmental reconstructions of poorly studied paleo-continents covering the Precambrian/Cambrian (PC/C) transition may improve the correlation of the events and their impact on the Earth system on a global scale. The Tarim Basin was presumably located proximal to the well-studied South China craton during the Ediacaran-Cambrian boundary and is expected to contribute equally to our paleoenvironmental reconstructions. Here we apply carbon and strontium (Sr) isotope records ($\delta^{13}C$ and $^{87}Sr/^{86}Sr$) obtained from well-preserved marine carbonates spanning the late Ediacaran to the late Cambrian from the Keping region in the northwestern Tarim Basin, NW China. By comparison to other carbonate successions from various paleo-continents, our obtained seawater $^{87}Sr/^{86}Sr$ curve in this study shows a stepwise first-order increase to more radiogenic values superimposed by second-order presumably regional variations. Our obtained $\delta^{13}C$ variations exhibit four prominent negative and three positive excursions identical to the global $\delta^{13}C$ record. Based on existing paleontological evidence and our new Tarim $\delta^{13}C$ and $^{87}Sr/^{86}Sr$ curves, we propose a stratigraphic correlation from the late Ediacaran to the late Cambrian between the Tarim Basin and other paleo-continents. Besides, our paleoenvironmental reconstruction reveals both regional and global sea-level changes that may have controlled the influx of radiogenic Sr and presumably the influx of nutrients controlling primary production and the rate of organic carbon burial in the Tarim Basin at the time of deposition. These feedbacks may have ultimately influenced the rapid diversification of metazoans and the oxygenation of the Cambrian ocean and atmosphere approaching-present pO_2 levels.

Keywords: Carbon isotopes, Strontium isotopes, Ediacaran-Cambrian, Tarim Basin, Paleoenvironment

1. Introduction

The transitional interval between the terminal Proterozoic and the early Paleozoic is marked by the sudden appearance of abundant and diverse metazoans (Valentine et al., 1999; Conway-Morris, 2003; Maloof et al., 2010; Kouchinsky et al., 2011). This early animal evolution was accompanied by extensive perturbations to climate, carbon (C) cycling, continental weathering and changes to the composition of the oceans (Shields-Zhou and Zhu, 2013). However, the cause-effect relationships between this evolutionary innovation and these environmental perturbations are still a matter of broad scientific debate and paleoenvironmental reconstructions of less studied paleo-continents covering the Precambrian/Cambrian (PC/C) transition can help this situation. Most studies from China covering this interval focus on sedimentary successions in South China. For instance, Li et al. (2013) suggested that muted continental weathering during the early Cambrian was indicated by decreasing seawater strontium isotope ratios ($^{87}Sr/^{86}Sr$). Ediacaran-Cambrian marine carbonate successions outcropping in the Tarim Basin were deposited on a shallow-water continental shelf, which was presumably situated close to the South China craton and at a similar low-middle latitude position (Fig. 1A) (McKerrow et al., 1992; Merdith et al., 2017; Huang et al., 2000; Zhan et al., 2007). In the past, Ediacaran-Cambrian Tarim Basin sediment successions have only received minor attention (Zhou et al., 2018; Zhu et al., 2019) but a few recent chemo-stratigraphic studies provided some preliminary results on their stratigraphic subdivision and paleoenvironmental conditions. He et al. (2007) and Guo et al. (2017) provided the first C isotope stratigraphic correlations for the late-Ediacaran Cambrian strata in the Tarim Basin between the Sugetbrak, the Penglaiba, the Wushi phosphorite and the Dongergou sections, while Wang et al. (2011b) presented paired C and Sr isotope trends from the Cambrian Series 2 to Series 3 at the Penglaiba section. However, there is still a chemo-stratigraphic gap (especially in regard of the Sr isotope stratigraphy) spanning the late-Ediacaran to the late-Cambrian time interval, which limits the stratigraphic correlation of the Tarim Basin with other parts of the world.

C and Sr isotope compositions obtained from well-preserved (i.e. low diagenetic fluid flow overprinted) ancient carbonate rocks may retain primary compositions of the

contemporaneous seawater and provide constraints on the isotope-based chemo-stratigraphic correlation (DePaolo and Ingram, 1985; Montañez et al., 1996; Montañez and Banner, 2000; Zhu et al., 2007; Wang et al., 2011b; McArthur et al., 2012; Li et al., 2013; Zhou et al., 2018; Zhu et al., 2019). For instance, the first appearance datum of small shelly fossils (SSFs) is globally accompanied by a negative $\delta^{13}C$ excursion and a declining trend in seawater $^{87}Sr/^{86}Sr$ ratios (Cowie and Glaessner, 1975; Landing, 1989; Zhu et al., 2006; Li et al., 2013; Zhu et al., 2019), although there are still debates about the exact boundary definition between the Ediacaran and the Cambrian (Geyer and Landing, 2017).

Secular variations in seawater $^{87}Sr/^{86}Sr$ ratios have been widely applied to reflect continental uplift, silicate weathering and variations in atmospheric carbon dioxide concentration (Burke et al., 1982; Keto and Jacobsen, 1987; Kaufman et al., 1993; Derry et al., 1994; Montañez et al., 1996; Denison et al., 1998; Montañez and Banner, 2000; Ebneth et al., 2001; Thomas et al., 2001; Melezhik et al., 2009; Sawaki et al., 2010). The $^{87}Sr/^{86}Sr$ ratio of seawater is controlled by a balance between continental weathering-derived Sr, hydrothermal Sr input and seafloor weathering (Palmer and Edmond, 1989). Continental source generally yields more radiogenic $^{87}Sr/^{86}Sr$ ratios due to the more radiogenic ^{87}Sr resulting from the excess decay of incompatible ^{87}Rb (rubidium) in evolved differentiated crustal rocks, while hydrothermal and seafloor weathering origin Sr deplete in radiogenic ^{87}Sr and therefore low $^{87}Sr/^{86}Sr$ ratios. Neglectable isotopic fractionation of the Rb/Sr system occurs during marine authigenic carbonate formation (Banner and Kaufman, 1994), together with its long residence time in the modern oceans, Sr is homogeneously distributed in the oceans and the seawater $^{87}Sr/^{86}Sr$ ratio ideally represents a global signature (DePaolo and Ingram, 1985). Thus, well-preserved marine carbonate minerals likely preserve the $^{87}Sr/^{86}Sr$ signature of the ambient seawater during the carbonate deposition.

In this study, we present C and Sr isotope compositions obtained in carbonates from the late Ediacaran to the late Cambrian at the Shiairik and Xiaoerbrak sections in the Keping region, Tarim Basin, NW China. The main objective of this study is to 1) document the variations of seawater C and Sr isotope compositions recorded in carbonates deposited in the Tarim Basin covering the late Ediacaran-late Cambrian interval; 2) refine the stratigraphic correlation of the sedimentary successions within the Tarim Basin; 3) interpret the data in the context of

115 reconstruction of continental weathering and sea-level changes. Our new interpretations
116 further aim to contribute to understanding of mechanisms linking environmental changes and
117 animal evolution during this critical period.
118
119 **2. Geological setting**
120
121 The Tarim Basin was presumably paleogeographically situated in a low to middle latitude
122 position between Australia and South China (see Fig. 1A) during the late Ediacaran to the late
123 Cambrian. Both Tarim and its adjacent South China craton developed widespread shallow
124 water carbonate platforms (McKerrow et al., 1992; Merdith et al., 2017; Huang et al., 2000;
125 Zhan et al., 2007). Our studied Keping region is located at the north-western Tarim Basin, NW
126 China (Fig. 1B) where the Ediacaran-Cambrian carbonate successions are outcropped at the
127 Xiaoerbrak and Shiairik sections (GPS locations: N 40° 55′ 23″, E 79° 53′ 53″ and N 40° 59′ 12″,
128 E 79° 59′ 35″ respectively).
129
130 **2. 1 Shiairik section**
131
132 The Shiairik section is located 30 km SW of Aksu city, NW Xinjiang Uygur Autonomous
133 Region (Fig. 1B). This section records an Ediacaran-Cambrian succession of more than 200 m
134 sedimentary rocks including the Ediacaran Sugetbrak and Chigebrak Formation (abbreviated
135 throughout the manuscript Fm.) as well as the Cambrian Yurtus Fm. The Ediacaran Chigebrak
136 and the overlying Cambrian Yurtus Fm. are separated by a disconformity between them (Fig.
137 2).
138 The Sugetbrak Fm. is mainly composed of reddish quartz sandstones interbedded with
139 mudstone and dolostone layers and is in conformable contact with the overlying Chigebrak Fm.
140 Rhythmic stratification, which reflects the influence of tidal currents, is widely developed in
141 the middle and upper part of the Sugetbrak Fm., suggesting a tidal flat depositional
142 environment (Deng et al., 2019). The Chigebrak Fm. contains thin-layered limestones
143 interbedded with brown sandstones at the bottom, overlain by medium-thick (10-50 cm)
144 layers of dolostones in the middle part and grey and yellowish medium-thick-layered

dolostones in the upper part (He et al., 2007; Wang et al., 2010).

The Chigebrak Fm. is in contact with the lower Cambrian Yurtus Fm. by a widely distributed unconformity in the Tarim Block (Wu et al., 2018). In the strata just below the unconformity, various features of karstification including breccias, cave-sediment infills, solution vugs and pores, were observed in the uppermost layers of dolostones in the Chigebrak Fm., indicating a possible erosional surface (He et al., 2018).

The lower Cambrian Yurtus Fm. mainly comprises black shales and phosphatic siliceous rocks with barite concretions, syn-genetic paleo-weathering crusts and abundant benthic SSFs (Qian and Xiao, 1984; Qian et al., 2000; He et al., 2007; Peng, 2009; Qian et al., 2009; Chen et al., 2010; Yao et al., 2014).

In the Shiairik section, 49 carbonate samples were collected from the 156 m-thick Ediacaran Chigebrak Fm. (n = 41) and the top part of the underlying Sugetbrak Fm. (n = 8), respectively (Fig. 2).

2. 2 Xiaoerbrak section

The Xiaoerbrak section is located 50 km SW of Aksu city, NW Xinjiang Uygur Autonomous Region and comprises more than 800 m sedimentary rocks subdivided in ascending stratigraphic order into the Cambrian Yurtus, Xiaoerbrak, Wusonger, Shayilik, Awatagh and Xiaqiulitagh Fm. (Fig. 1 & 2), which are stratigraphically continuous without any depositional gaps.

The 21 m thick Yurtus Fm. is subdivided into two parts: the lower Yurtus Fm. consists of black shales, phosphatic siliceous rocks with the occurrence of sponge spicules (Peng, 2009; Chen et al., 2010) and rare SSFs (*Protohertzina Anabarica Missarzhevsky* and *Anabarites* (Zhou and Chen, 1990; Zhou, 2001), Fig. 2), while the upper part comprises thin-layered (1-10 cm) siliceous dolostones and muddy dolostones containing abundant SSFs (Qian and Xiao, 1984; Zhou and Chen, 1990; Qian et al., 2000; Zhou, 2001; Qian et al., 2009; Chen et al., 2010), such as *Paragloborilus Spinatus* (Qian and Xiao, 1984) and *Lapworthella* (Zhou and Chen, 1990). The sedimentary facies of the Yurtus Fm. are described in the literature as deposited in a restricted basin environment inferred from sedimentologic and geophysical studies as well as from

molybdenum isotope compositions analyzed in the Yurtus black shales (Bai et al., 2019; Yao et al., 2014; Yao et al., 2017; Yu et al., 2009).

The conformably overlying Xiaoerbrak Fm. consists of 138 m-thick medium-thick layered micritic dolostone, which hosts three trilobite assemblages (in ascending stratigraphic order: *Shizhudiscus* Zone, *Metaredlichioides* or *Ushbaspis* Zone, *Kepingaspis-Tianshanacephalus* Zone) (Wang et al., 1985; Zhou and Chen, 1990; Zhou, 2001; Peng, 2009; Fig. 2).

The 95 m-thick Wusonger Fm. is mainly composed of fine-grained micritic dolomites and muddy dolostones (Sun et al., 2004; Yu et al., 2004; Wang et al., 2010). Fossils of *Paokannia* considered to survive from the Cambrian late Stage 3 to the end of Cambrian Series 2 were identified in this formation (Zhou, 2001; Peng, 2009, Fig. 2 orange arrow indicates fossil range). Semi-restricted carbonate platforms were indicated from thin-section studies of the muddy dolostone (Bai et al., 2019).

The overlying Shayilik Fm. contains the *Kunmingaspis-Chittidilla* biozone and comprises micritic and fine-grained dolomites in the lower part, dolomite-bearing limestones in the upper part, and is topped by algal microbialites (Zhou, 2001; Peng, 2009, Fig. 2 yellow arrow indicates fossil range).

The Awatagh Fm. spans about 200 m and comprises anhydrite and anhydrite-bearing dolostones at the bottom overlain by purple medium-thin (5-30 cm) bedded micritic dolomites and fine-grained dolomites in the upper part. Bai et al. (2019) studied the sedimentary characteristics of the Shayilik and Awatagh Fm. and proposed their sedimentary environments experienced a transgression and changed from gentle slope environments to restricted platforms. The overlying Xiaqiulitagh Fm. mainly consists of dolomites, intercalated with stromatolitic dolomites (Wang et al., 2011b) and siliceous dolomites exposed in the middle part of this Fm.

At the Xiaoerbrak section, 126 carbonate samples and three phosphorite samples were collected (Fig. 2). Based on regional lithostratigraphic and biostratigraphic correlation as well as sedimentary facies comparison, Shiairik and Xiaoerbrak sections are integrated into one single lithological succession in this study (Fig. 1B).

3. Analytical methods

Hand specimen free from visible alteration such as weathering crusts and visible calcite veins were collected in the field and subsequently crushed into small pieces of ~0.5 cm diameter. The best-preserved pieces (i.e. showing no microscopic calcite veins) were handpicked and ground into fine powder in an agate mill (200 mesh) for further geochemical analyses.

0.5 mg of sample powders were baked for ten hours at 70 °C and then reacted with orthophosphoric acid at 70 °C for 1.5 hours to extract CO_2 (McCrea, 1950; Craig, 1953) for subsequent measurement of C and oxygen (O) isotope compositions. C and O isotope compositions were determined using a Gas-isotope ratio mass spectrometer (IRMS) of type Finnigan Delta Plus XP at the State Key Laboratory for Mineral Deposits Research, Nanjing University, China. Chinese carbonate reference materials (TTB-1 and TTB-2) were analyzed along with our samples for isotopic calibration and to test for memory effects. C and O isotope compositions were measured relative to analyses of an in-house standard and the obtained data is here expressed relative to the international V-PDB (Vienna Pee Dee Belemnite) reference material against which our in-house standard was calibrated. We use the δ notation throughout the manuscript, which is the permille deviation of the C and O isotope compositions from the V-PDB reference material. The analytic precision of our method was determined on repeated analyses of the external reference materials and is in the order of ±0.15 ‰ for $\delta^{13}C$ and ±0.1 ‰ for $\delta^{18}O$ respectively (2SE) (Table 1).

For the measurements of the concentrations of calcium (Ca), magnesium (Mg), manganese (Mn), Sr and Rb in the carbonate fraction of the studied samples, ~50 mg of sample powder was weighed into a 15 ml centrifuge tube. First, 3 ml 1 M sub-boiling double-distilled acetic acid (HAc) were added and the tubes placed in an ultrasonic bath for 30 minutes. Then the samples reacted at room temperature for 12 hours in order to sufficiently dissolve carbonate minerals. Finally, the solutions were centrifuged for 15 minutes at 4000 rpm, and the supernatant was placed into a 15 ml PFA beaker.

Subsequently, 2 ml ultrapure water was added into the 15 ml centrifuge tube to wash the remaining residue. After being placed in an ultrasonic bath for another 30 minutes and centrifugation for 15 minutes, the supernatant solutions were added into the 15 ml PFA

beakers and this rinsing step was repeated. The combined 7 ml of supernatant (dissolved carbonate fraction) were then dried down at 120 °C and re-dissolved in 3% v/v double-distilled nitric acid with a dilution factor of 1:1000 for concentration measurements (the detailed dissolution procedure summarized in Fig. 3). Mn, Sr and Rb concentrations were determined using a Thermo Finnigan Element XR sector-field ICP MS at the State Key Laboratory for Mineral Deposits Research (Nanjing University, PR China) with a Scott type quartz spray chamber and a 100 µl/min nebulizer. For instrument drift correction, we doped 10 ppb rhodium into the sample solutions for elements analyzed in low-resolution mode. The Ca and Mg concentrations were determined using a Sky-ray ICP OES at the same laboratory. Along with the ICP OES analyses and the ICP MS analyses, a dolomite reference material (JDo-1) was repeated one time per 10 analyses, the repeated analyses of JDo-1 on ICP MS and ICP OES yielded < 10 % accuracy and < 5 % precision.

Samples with relatively high Sr concentrations and low Mn/Sr ratios were selected for Sr isotope measurements. Solutions containing around 20 ng Sr were dried at 120 °C and dissolved in 1 ml 3 M double-distilled nitric acid followed by standard Sr-spec resin ion-chromatography for Sr purification. Sr isotope compositions were obtained on an MC-ICP-MS (Thermo Neptune Plus) at the State Key Laboratory for Mineral Deposits Research in Nanjing University, China. Mass fractionation was corrected by applying an assumed $^{86}Sr/^{88}Sr$ ratio = 0.1194 and the exponential law (Nier, 1938). The NIST SRM 987 standard was analyzed along with the samples and yielded a mean value of 0.710271±30 (2SE, n= 30). The Sr isotope ratios and their corresponding standard error of the mean are listed in Table 1. Data mentioned in the text has been normalized to the recommended NIST SRM 987 standard value of 0.710248 (McArthur et al., 2012).

4. Results

4.1 C isotope feature at the Precambrian/Cambrian (PC/C)

All C isotope data obtained on carbonate leachates are reported in the delta (δ) notation relative to V-PDB and the $\delta^{13}C$ values of all analyzed carbonate samples are plotted in Fig. 4 and tabulated in Table 1, respectively. The $\delta^{13}C$ values fluctuate between -13.3 ‰ and +7.9 ‰.

265 The $\delta^{13}C$ curve obtained in carbonates from the Sugetbrak Fm. to the Xiaquilitagh Fm. shows
266 four prominent negative excursions ("B", "C", "E", "F", Fig. 4, here we define "excursion" as a
267 visible deviation, i.e. more than 10 % offset from their pre-excursion background values) and
268 three positive excursions ("A", "D", "G", Fig. 4).

269 The first $\delta^{13}C$ positive excursion appears at the boundary between the Chigebrak Fm. and
270 Sugetbrak Fm. In this interval, the $\delta^{13}C$ values increase from -5.5 ‰ to +7.9 ‰ (Fig. 4, positive
271 excursion "A"), and then plunge down to ~+1 ‰ resulting in a small negative excursion (Fig. 4,
272 negative excursion "B"). Above the negative excursion "B", the $\delta^{13}C$ values increase to a steady
273 background value around +2.5 ‰ through the rest of the Chigebrak Fm.

274 The $\delta^{13}C$ values increase from -2.5 ‰ to +0.5 ‰ in the lower part of the Yurtus Fm.,
275 decrease rapidly to -5.1 ‰ in the middle part ("C-1", Fig.4), and then increase again to +0.9 ‰
276 over a short interval in the upper part of the Yurtus Fm. ("C-2", Fig. 4). At the top of the Yurtus
277 Fm., the $\delta^{13}C$ values slowly decrease to -0.5 ‰ ("C-3", Fig. 4).

278 The whole Xiaoerbrak Fm. demonstrates a prolonged positive C excursion ("D", Fig. 4, $\delta^{13}C$
279 values vary from -0.5 ‰ to +3 ‰) with two negative swings. One occurs at the base of the
280 Xiaoerbrak Fm., varying from +2.5 ‰ to +1.7 ‰, and then recovers to +3 ‰ ("D-1", Fig. 4). The
281 other negative excursion occurs in the middle part of the Xiaoerbrak Fm., decreasing from +3 ‰
282 to +1.8 ‰, and then recovering to +2.5 ‰ ("D-2", Fig. 4).

283 At the boundary between the Wusonger and the Xiaoerbrak Fm., the $\delta^{13}C$ values gradually
284 decrease to ~0 ‰ followed by a plunge to -2.0 ‰. The $\delta^{13}C$ values subsequently recover to
285 ~0 ‰ at the top of the Wusonger Fm., completing the negative excursion "E" (Fig. 4). The $\delta^{13}C$
286 values decrease sharply to a prominent negative nadir of -13.3 ‰ forming the most negative
287 excursion "F" in our dataset (Fig. 4) at the bottom of the Shayilik Fm. In the upper part of the
288 Shayilik Fm., the $\delta^{13}C$ values recover to ~0 ‰.

289 A $\delta^{13}C$ positive excursion (Fig. 4, positive excursion "G") varying from -1.5 ‰ to +1.5 ‰
290 was identified in the mid-upper part of the Awatagh Fm. The positive excursion "G" consists
291 of positive excursion "G-1" (varying from -1.5 ‰ to +1.5 ‰) and "G-2" (varying from -1.5 ‰
292 to 0 ‰). Subsequently, almost the entire Xiaqiulitagh Fm. sustains a constant $\delta^{13}C$ value at ~-
293 1.0 ‰ with a minor rise to ~0 ‰ at the top of this formation.

294

295 **4.2 O isotope compositions at the PC/C**

296

297 The here presented O isotope data are obtained on carbonate leachates and reported in
298 the delta (δ) notation relative to V-PDB. The $\delta^{18}O$ values of the analyzed carbonates are plotted
299 in Fig. 4 and tabulated in Table 1. The $\delta^{18}O$ values from the Ediacaran samples (from the Shiairik
300 section) systematically differ from those obtained in the Cambrian samples (from the
301 Xiaoerbrak section) (Fig. 4). The $\delta^{18}O$ values in the Ediacaran stratigraphic units range from -
302 9 ‰ to 0 ‰ and have a mean value of -3 ‰. By contrast, almost all samples in the Cambrian
303 units have $\delta^{18}O$ values ranging from -12 ‰ to -3 ‰ (mean= -7 ‰) except some samples in the
304 Yurtus Fm. which show more negative values.

305 Sawaki et al. (2010) reported $\delta^{18}O$ values ranging from -10 ‰ to 0 ‰, averaging at -4 ‰
306 for the Ediacaran Three Gorges area, South China. Besides, Wang et al. (2011b) obtained $\delta^{18}O$
307 values ranging from -7.9 ‰ to +3.5 ‰ through the Cambrian Series 2 to Series 3 in the
308 Penglaiba section of the Keping region. Thus, our $\delta^{18}O$ values of the two studied section are
309 generally consistent with existing Ediacaran and Cambrian datasets.

310

311 **4.3 Sr isotope compositions at the PC/C**

312

313 Samples selected for Sr isotope measurements yield low $^{85}Rb/^{86}Sr$ ratios (all samples <
314 0.0016) (Table 1), suggesting that the chromatographic Sr separation from matrix elements
315 using the specific Sr resin was effective. Further, samples with low Mn/Sr ratios (< 5) and
316 relatively high Sr concentrations (generally > 50 ppm) were selected to perform Sr isotope
317 analyses to minimize possible influence of diagenetic alteration (see discussion in section
318 5.1.2).

319 As shown in Fig. 4, the obtained $^{87}Sr/^{86}Sr$ ratios in our carbonate leachates vary between
320 0.7085 and 0.7102. From the uppermost part of the Sugetbrak Fm. to the middle Chigebrak
321 Fm., the $^{87}Sr/^{86}Sr$ values decrease from ~0.7095 to ~0.7085. Then the $^{87}Sr/^{86}Sr$ values increase
322 to ~0.7090 at the top of the Chigebrak Fm.

323 In the Yurtus Fm., the $^{87}Sr/^{86}Sr$ ratios change rapidly within the range of 0.7086 to 0.7102,
324 followed by a plateau at ~0.7088 through most of the Xiaoerbrak Fm. Finally, a rise to ~0.7090

at the top of the Xiaoerbrak Fm. coincides with the positive $\delta^{13}C$ excursion "D" and a $\delta^{13}C$ platform at 0 ‰ above the excursion "D". In the Wusonger Fm., the $^{87}Sr/^{86}Sr$ ratios rise slowly from ~0.7088 to ~0.7090 and sharply increase to 0.7092 at the bottom of the Shayilik Fm.

At the bottom of the Shayilik Fm., the recorded $^{87}Sr/^{86}Sr$ ratios drop to ~0.7087, coinciding with the prominent negative $\delta^{13}C$ excursion "F". Subsequently, the $^{87}Sr/^{86}Sr$ ratios gradually increase to ~0.7092 in the mid-upper part of Awatagh Fm., coinciding with the rising limb of the positive $\delta^{13}C$ excursion "G". Apart from only one outlier at 0.7086 in the lower part of Xiaqiulitagh Fm., the $^{87}Sr/^{86}Sr$ ratios recorded in carbonates from the rest of the Cambrian (i.e. Xiaqiulitagh Fm. and Upper Awatagh Fm.) is constant at ~0.7091.

5. Discussion

5.1 Assessing possible processes altering the C/Sr isotope compositions

5.1.1 The effect of silicate leaching and dolomitization on the $^{87}Sr/^{86}Sr$

To evaluate the influence of possible silicate leaching with our digestion method on the obtained $^{87}Sr/^{86}Sr$ ratios, a cross plot of $^{87}Sr/^{86}Sr$ versus [Rb] (i.e. Rb concentration normalized by CaO+MgO) is provided in the Fig. 6G and 6N. The absence of apparent correlations between Sr concentrations as well as $^{87}Sr/^{86}Sr$ ratios and [Rb] indicates our digestion method avoids substantial silicate mineral leaching as these contain much higher Rb contents and more radiogenic Sr than carbonate minerals. Moreover, there are no apparent correlations in all analyzed carbonates in the cross plots of $^{87}Sr/^{86}Sr$-Mg/Ca and $^{87}Sr/^{86}Sr$-carbonate content (%) (Fig. 6E, 6F, 6L, 6M), indicating $^{87}Sr/^{86}Sr$ ratios may not be influenced by dolomitization. Thus, we consider our sample digestion method as a suitable method to treat ancient marine carbonates, and our obtained $^{87}Sr/^{86}Sr$, $\delta^{18}O$ and $\delta^{13}C$ values as suitable proxies to record ambient seawater compositions (section 5.1.2 and 5.1.3).

5.1.2 The influence of diagenetic alteration

Any possible diagenetic overprint superimposed on the primary geochemical seawater

signatures of marine carbonates (e.g. late-stage fluid alteration causing carbonate dissolution and reprecipitation) requires to be examined in detail, and any altered samples need to be rigorously screened out. In general, typical chemical characteristics of carbonates that experienced a high degree diagenetic alteration yield elevated Mn/Sr ratios, low $\delta^{18}O$ values and possibly low $\delta^{13}C$ values and elevated $^{87}Sr/^{86}Sr$ ratios (e.g. Marshall, 1992; Kaufman et al., 1993; Derry et al., 1994). Thus, cross-plots of Mn/Sr ratios, $\delta^{18}O$, $\delta^{13}C$ and $^{87}Sr/^{86}Sr$ ratios are useful and widely used tools to evaluate the degree of alteration. Moreover, Mn/Sr ratios and $\delta^{18}O$ values are considered useful diagnostic tools of late-stage alteration of water-rock interaction (Marshall, 1992; Derry et al., 1994; Kaufman and Knoll, 1995). Almost all the dolostone samples in this study, as well as those from other sections in the Keping area (e.g. Guo et al., 2017), have low Sr concentrations (< 300 ppm) which is possibly indicative for low initial seawater Sr concentrations at the time of deposition (cf. Li et al., 2011). Here we selected more generous cut-offs for our studied dolostone samples during our pre-screening: samples that clearly deviate from the main data group (Mn/Sr > 5 and $\delta^{18}O$ < -10 ‰, Fig. 5) are considered as not representing primary seawater $^{87}Sr/^{86}Sr$ signals (Derry et al., 1994; Kaufman and Knoll, 1995; Li et al., 2013; Zhou et al., 2020).

Nearly all Ediacaran samples show isotopically heavier $\delta^{18}O$ values (> -10 ‰) and lower Mn/Sr (< 5) (Fig. 5). However, carbonates from the Sugetbrak Fm. show a positive correlation between $\delta^{18}O$ and $\delta^{13}C$ (R^2 = 0.95; Fig. 5A). Besides, correlations between radiogenic $^{87}Sr/^{86}Sr$ ratios and low $\delta^{13}C$ and $\delta^{18}O$ values are present (R^2 = 0.89 and 0.95 respectively; Fig. 6H and 6I), suggesting that the Sugetbrak Fm. might have suffered substantial diagenetic alteration by basin-type fluids which enriched in “light” C and O and radiogenic Sr isotopes (see Hohl et al., 2015b).

Most Cambrian samples show no apparent correlations in the cross-plot of $\delta^{13}C$ versus $\delta^{18}O$ (Fig. 5B). However, carbonate leachates of the Yurtus Fm. show elevated Mn/Sr ratios (> 5; circles in Fig. 6D) and a positive correlation between $^{87}Sr/^{86}Sr$ ratios and $\delta^{18}O$ values (Fig. 6B), which indicates that the obtained Sr isotope compositions in the Yurtus Fm. have been influenced by the mixing of restricted basin Sr signals with less radiogenic fluids (see section 5.1.3). However, the obtained $\delta^{13}C$ values in the Yurtus Fm. carbonates show no correlation with obtained $^{87}Sr/^{86}Sr$ and $\delta^{18}O$ values (Fig. 6A and 5B), suggesting that the carbonates in the

Yurtus Fm. likely preserved the primary seawater C isotope composition.

In the Wusonger Fm., the $\delta^{18}O$ value of one sample yields -10 ‰ and its $\delta^{13}C$ value is similarly low (-6.7 ‰) (Fig. 5B). Therefore, the sample is excluded from the seawater C and Sr evolution curve (in sections 5.2 and 5.3). Likewise, the $\delta^{18}O$ value of another data point in the Shayilik Fm. is lower than -10 ‰. However, no paired decrease in the $\delta^{13}C$ excludes the possibility of significant post-depositional fluid alteration for this sample.

Apart from these obviously altered samples, there is no clear correlation in the cross-plots of $\delta^{18}O$-$\delta^{13}C$ (Fig. 5), $^{87}Sr/^{86}Sr$-$\delta^{18}O$, $^{87}Sr/^{86}Sr$-$\delta^{13}C$, $^{87}Sr/^{86}Sr$-[Sr], $^{87}Sr/^{86}Sr$-Mn/Sr, $^{87}Sr/^{86}Sr$-Mg/Ca and $^{87}Sr/^{86}Sr$- Carbonate content (%) (Fig. 6). Thus, we consider these samples are well-preserved marine carbonates, of which their $^{87}Sr/^{86}Sr$ and $\delta^{13}C$ values may record primary seawater compositions.

5.1.3 Fluid mixing model for Sr isotope compositions in the Yurtus Fm.

Samples of the Yurtus Fm. show elevated Mn/Sr ratios (> 5; circles in Fig. 6D), arguing for excess in Mn possibly due to pore water-redox controlled remobilization of MnO colloids (Cowie et al., 1995; Thomson et al., 1998; Hohl et al., 2017). Besides, carbonate leachates of the Yurtus formation show a positive correlation between $^{87}Sr/^{86}Sr$ ratios and $\delta^{18}O$ values (Fig. 6B) with two endmembers, one with the least-radiogenic $^{87}Sr/^{86}Sr$ ratios and light $\delta^{18}O$ values, while the other endmember has more radiogenic Sr and heavier O isotopic compositions. However, diagenetic basin-type fluid-alteration usually results in a negative correlation between $^{87}Sr/^{86}Sr$ ratios and $\delta^{18}O$ values (Hohl et al., 2015b).

In order to explore the mechanisms that may generate the full range in O and Sr isotope compositions observed in the Yurtus Fm., a simple open-system fluid mixing model (Jacobsen and Kaufman, 1999) is applied. As inferred from the paired Sr and O isotope results, two endmembers have been identified: one is a radiogenic localized basin-type seawater ($^{87}Sr/^{86}Sr$ = 0.7102, $\delta^{13}C$ = 0.5 ‰, $\delta^{18}O$ = 0.5 ‰ and Sr = 50 ppm), while the other endmember is a meteoric fluid with $^{87}Sr/^{86}Sr$ of 0.7085, $\delta^{13}C$ of -5 ‰, $\delta^{18}O$ of -14 ‰ and 600 ppm Sr (Fig. 6A, 6B and 6C). Data of the Yurtus carbonates falls on a mixing trend line between the localized

seawater and a lighter $\delta^{18}O$ bearing meteoric fluid, exhibiting mixing ratios between 0.01 to 5 (Fig. 6A, 6B, 6C).

In general, meteoric fluids comprise more radiogenic Sr and lower Sr concentrations than contemporaneous seawater (e.g. Xu and Han, 2009). However, the hypothetic global regression at the Precambrian/Cambrian boundary presumably causing the 'great unconformity' (Brasier, 1996; Ishikawa et al., 2008; Sawaki et al., 2008; He et al., 2017) might have exposed extensive amounts of Precambrian marine carbonates on the shelf, and thus, meteoric fluids leaching these lithologies, might have inherited their Ediacaran seawater-like Sr isotopic compositions and Sr concentrations. He et al. (2018) suggested a wide geographical distribution of paleo-karsts at the top of the Chigebrak Fm. and speculated that there is an Ediacaran carbonate paleo-upland adjacent to the Xiaoerbrak and Shiairik sections during this time interval. Furthermore, similar Sr isotope composition and Sr concentration of the Chigebrak Fm. carbonates with those of our modelled meteoric fluid ($^{87}Sr/^{86}Sr$ ratio ~0.7085; Sr concentration ~600 ppm) argue for a contribution to the carbonate $^{87}Sr/^{86}Sr$ in the Yurtus Fm. from such an endmember.

On the other hand, the Sr isotope composition of the seawater endmember (~0.7102) in this study is more radiogenic when compared to the reported $^{87}Sr/^{86}Sr$ seawater ratio from the correlative strata in South China (~0.7085, Li et al., 2013), which may be explained by a local rather than global signature, arguing for a restricted basin depositional environment on the shelf of the Tarim craton during this period (cf. Bai et al., 2019; Yao et al., 2017).

Several syn-genetic ancient weathering crusts in the Yurtus Fm. imply subaerial exposure environments and the occurrence of black shale in the lower part of the Yurtus Fm. indicate facies change to deep-water deposition. Hence the two depositional settings probably represent sea-level fluctuations. Because the early Cambrian Tarim Basin was presumably restricted and underwent several second-order sea-level shifts (Yao et al., 2017), we argue that meteoric fluids leaching from aerial exposed Ediacaran shelf carbonates are mixed with confined basin waters. The basin may be localized at the late-Ediacaran and the basin water may be influenced by enhanced silicate weathering of hinterland during the global regression at the late-Ediacaran (Haq and Schutter, 2008).

443 **5.2 C isotope stratigraphic and bio-stratigraphic correlation**

444

445 Before performing a stratigraphic correlation between the Tarim block and other time-
446 equivalent paleo-continents, it is essential to note that our obtained C isotope variation curve
447 can be correlated to the existing datasets from other sections in the Tarim Basin. For example,
448 similar rapid increasing $\delta^{13}C$ trends in the top part of the Sugetbrak Fm. have been reported at
449 a composite profile from seven sections in the Quruqtagh area and at the Penglaiba section in
450 the Keping area by Xu et al. (2003) and He et al. (2007), respectively. Further, Guo et al. (2017)
451 reported extreme negative $\delta^{13}C$ values (down to -14.3 ‰) at the boundary of the
452 Wusonger/Shayilik Fm. in the Penglaiba section in the Keping area, similar to our negative $\delta^{13}C$
453 excursion "F" with respect to the total magnitude of the excursion (down to -13.3 ‰).
454 During the PC/C, the Tarim Basin was situated in a low latitude location on the continental
455 margin shelf (Yu et al., 2009), leading to the deposition of shallow water carbonate sediments.
456 This makes the Tarim Basin sections lithologically and paleogeographical similar to other
457 shallow marine PC/C sections on the Yangtze Platform (McKerrow et al., 1992; Merdith et al.,
458 2017; Huang et al., 2000; Zhan et al., 2007; Hohl et al., 2015a). Therefore, we here apply the
459 Ediacaran/Cambrian bio-chemostratigraphic division of South China as the primary reference
460 frame for the correlation with our studied bio-chemostratigraphic data from the two sections.
461 Fig. 7 shows the carbonate C isotope evolution curve from the Keping region and our proposed
462 C isotope stratigraphic correlation with the reported composite carbonate C isotope evolution
463 curves of South China from the late Ediacaran (Jiang et al., 2007), across the Ediacaran-
464 Cambrian transition (Li et al., 2013), and through the Cambrian Series 2 to Series 3 (Guo et al.,
465 2010). On a global scale, we also compare our Tarim Basin carbonate C isotope evolution curve
466 with records from North India during late Ediacaran (Kaufman et al., 2006) and the Cambrian
467 global seawater standard $\delta^{13}C$ variations proposed by Zhu et al. (2006), which is mainly derived
468 from South China shallow-water carbonates. Similarly, carbonate C isotope datasets from
469 Laurentia (Montañez and Banner, 2000) and Siberia (Wotte et al., 2011) spanning the
470 Cambrian Series 2 – Series 3 strata and carbonate C isotope data from Southwest Mongolia
471 spanning the Ediacaran-Cambrian transition (Brasier et al., 1996) are used for correlation.
472 According to the current Ediacaran chronostratigraphy proposed by Zhu et al. (2007), the

upper Doushantuo negative $\delta^{13}C$ excursion (DOUNCE, equivalent to the Shuram/Wonoka excursion) ranges from ca. 560 Ma to 551 Ma and the following positive $\delta^{13}C$ excursion that ended at around 548 Ma, which provide a general baseline reference for C isotope stratigraphy in the mid-late Ediacaran. In South China, a sharp $\delta^{13}C$ rise predates the positive $\delta^{13}C$ excursion at the boundary between the Doushantuo and the Dengying Fm. (e.g. Jiang et al., 2007). Similar $\delta^{13}C$ variations were observed at the boundary between the Sugetbrak and Chigebrak Fm. in the Tarim Basin which lead to the hypothesis that the Chigebrak Fm. is stratigraphically equivalent to the Dengying Fm. in South China (He et al., 2007). The studied Shiairik section is merely 40 km away from the site investigated by He et al. (2007) and similarly obtained carbonate $\delta^{13}C$ curves at both sites suggest that the Chigebrak carbonates have only experienced minimal diagenetic alteration and thus, may archive the $\delta^{13}C$ signals of coeval Ediacaran paleo-seawater. As mentioned above, the positive excursion "A" occurring at the boundary between the Chigebrak and Sugetbrak Fm. is consistent with the Ediacaran division plan proposed by Zhu et al. (2007) and He et al. (2007). Since, late Ediacaran South China strata bears no other obvious negative $\delta^{13}C$ excursion above the ca. 548 Ma old positive $\delta^{13}C$ excursion (Fig. 7I) while North Indian strata of the same time reveals two negative $\delta^{13}C$ excursions (Fig. 7J), the negative excursion "B" obtained in the Tarim Basin carbonates cannot be considered as a global $\delta^{13}C$ excursion.

A slight $\delta^{13}C$ decline at the top of Chigebrak Fm. is similar to the $\delta^{13}C$ excursion at the top of the Dengying Fm. (Fig. 7I) and a subsequent sharp decrease (negative Excursion "C") across the top of the Chigebrak Fm. and the lower Yurtus Fm. is suggested as equivalent to the globally identified BACE (BAsal Cambrian C isotope Excursion) (Fig. 7B, 7G, 7H). This interpretation is consistent with previous studies in which the parallel unconformity between the Chigebrak Fm. and the Yurtus Fm. is considered to represent the boundary between the Ediacaran and Cambrian in the Tarim Basin (Yao et al., 2014; He et al., 2018).

The appearance of SSFs, that are widely distributed during the Terrenenvian Series (Zhu et al., 2006), can further be used for robust biostratigraphic correlation. In South China, the *Anabarites-Protohertzina-Arthochites* assemblage, the first Terreneuvian SSFs assemblage in the Southwest Chinese Province of Yunnan, agrees well with the earliest skeletal faunas on the Siberian Platform and the Canadian Cordillera (Qian and Bengtson, 1989; Steiner et al., 2004;

Yang et al., 2014a; Yang et al., 2014b). The lower Yurtus Fm. in the Tarim Basin, which contains an *Anabarites-Protohertzina* assemblage (Qian and Xiao, 1984), can be correlated to the lower Terreneuvian. Moreover, because the second assemblage (*Siphogonuchites-Paragloborilus*) and the last assemblage (*Lapworthella-Tannuolina-Sinosachites*) found in Yunnan (Qian and Xiao, 1984; Qian and Bengtson, 1989; Yang et al., 2014a) also appear in the upper Yurtus Fm. (i.e. *Paragloborilus-Lapworthella* assemblage), we suggest that all or most of the Yurtus Fm., conformably underlying the trilobite-bearing Xiaoerbrak Fm. can be best assigned to the Terrenenvian Series.

The Terrenenvian Series (the first series of the Cambrian) is characterized by more than three carbonate $\delta^{13}C$ excursions recorded in South China sections, i.e. BACE, ZHUCE (ZHUjiaqing C isotope Excursion) and SHICE (SHIyantou C isotope Excursion) (Fig. 7B). One negative $\delta^{13}C$ excursion (Fig. 4, "C-2") and two positive $\delta^{13}C$ excursions (Fig. 4, "C-1" and "C-3") are recorded in the Yurtus Fm. carbonates, not perfectly matching the reported excursions' amounts and magnitudes during the Terreneuvian epoch in South China. As syn-genetic ancient weathering crusts were recognized in field observation, several depositional hiatuses in the Yurtus Fm. may explain the differences in the early Cambrian $\delta^{13}C$ profiles between South China and the Tarim Basin.

The Cambrian Stage 3 is marked by the first appearance of trilobites and two positive $\delta^{13}C$ excursions (Cambrian Arthropod Radiation isotope Excursion (CARE) and MIngxinsi C Isotope Excursion (MICE), Zhu et al., 2006). Due to the appearance of *Shizhudiscus* at the bottom of the Xiaoerbrak Fm., it may be assigned to the base of the Cambrian Series 2. Besides, due to the consistency in $\delta^{13}C$ variation trends (a major positive excursion with a sub-negative excursion) and magnitudes (increase from ~0 ‰ to +3 ‰) between the upper part of the positive $\delta^{13}C$ excursion "D" (with the sub-negative excursion "D-2") and the MICE (Fig. 7), this study correlates the upper part of the excursion "D" as equivalent to the MICE in South China. Although the lower part of the excursion "D" is not perfectly matching in shape to the CARE, the similar magnitude of the excursion "D-1" (decreasing from +2.5 ‰ to +1.7 ‰) and the appearance of *Shizhudiscus* broadly confirms that the negative $\delta^{13}C$ excursion "D-1" likely corresponds to the falling limb of the CARE. Therefore, combining the evidence that the appearance of *Shizhudiscus* occurs slightly later than the start of the Cambrian Series 2 (Fig.

7B, the green arrow represents the strata with *Shizhudiscus* occurrence), the boundary between the Yurtus Fm. and the Xiaoerbrak Fm. is considered to be stratigraphically higher than the base of the Cambrian Stage 3 in the Tarim Basin.

The ROECE (Redlichiid–Olenellid Extinction C isotope Excursion; Zhu et al., 2006), the most negative $\delta^{13}C$ excursion throughout the Cambrian Series 2 to Furongian (Fig. 7C, 7D, 7E, 7F, e.g. Fan et al., 2011; Guo et al., 2017), is considered to represent the boundary between the Cambrian Stage 4 and the Wuliuan Stage (Montañez and Banner, 2000; Zhu et al., 2006; Guo et al., 2010; Wotte et al., 2011; Guo et al., 2017). Accordingly, we consider that the most negative $\delta^{13}C$ excursion "F" in our studied carbonates is equivalent to the ROECE and the bottom of the Shayilik Fm. probably represents the base of the Cambrian Series 3 (Fig. 7). This correlation is consistent with the stratigraphic correlations by Guo et al. (2017) and Wang et al. (2011b) and the appearance of the *Kunmingaspis-Chittdilla* (Fig. 2) in the Shayilik Fm. (Zhou, 2001; Peng, 2009), the biozone range of which overlaps with the Wuliuan Stage (Wang et al., 2011a, Fig. 7, the yellow arrow represent the strata with *Kunmingaspis-Chittdilla* occurrence). Below the negative $\delta^{13}C$ excursion "F", by comparing the $\delta^{13}C$ variation magnitude, the negative $\delta^{13}C$ excursion "E" in the Wusonger Fm. may be equivalent to the Archaeocyathid Extinction C isotope Excursion (AECE, Zhu et al. (2006)). This hypothesis is further supported as *Paokannia* is considered to survive from mid-Cambrian Series 2 (late Stage 3) to the end of Cambrian Series 2 (Zhou, 2001; Peng, 2009) (Fig. 7, the orange arrow represents the *Paokannia*-bearing strata).

The positive $\delta^{13}C$ excursion "G" is the only apparent positive excursion overlying the negative $\delta^{13}C$ excursion "F", and this temporal distribution is similar to the chronological order between SPICE (Steptoean C-Isotope Positive Excursion) and ROECE. However, the positive $\delta^{13}C$ excursion "G" is not as distinct as the SPICE reported from other paleo-continents and its magnitude of 3‰ is smaller than the magnitude of the SPICE recorded elsewhere (~4-6‰) (Li et al., 2018), which may suggest depositional hiatuses existing at the base of the Furongian in the Keping area. Considering that no depositional hiatus is reported in the Awatagh Fm., we tentatively speculate that the positive excursion "G" is identical to SPICE but suggest further verification by independent sedimentological and geochemical proxies. Because the SPICE is the typical characteristic of the start of the Paibian stage of the Furongian Series (Saltzman et

al., 1998; Peng et al., 2004; Zhu et al., 2006; Fan et al., 2011), a correlation of the positive excursion “G” with SPICE would mean that the upper Awatagh Fm. in the NW Tarim Basin may be preliminarily assigned to the Furongian Series.

5.3 Sr isotope stratigraphic correlation

Based on the carbonate C isotope stratigraphic correlation, a carbonate-based seawater $^{87}Sr/^{86}Sr$ curve (Fig. 8 red dashed line) is constructed using a “lower limit” Sr isotope data approach (Jones et al., 1994). Fig. 8 shows the obtained least-diagenetically altered $^{87}Sr/^{86}Sr$ ratios from carbonate leachates in the Tarim Basin of this study (Fig. 8D), a proposed standard Cambrian global seawater $^{87}Sr/^{86}Sr$ curve (Fig. 8A, Peng et al., 2012; Zhu et al., 2019) constructed after the work of Derry et al. (1994); Montañez and Banner (2000); Ebneth et al. (2001); Kouchinsky et al. (2008) as well as the $^{87}Sr/^{86}Sr$ values recorded in carbonates from the Yangtze Platform, South China during the Ediacaran-Cambrian transition period (Fig. 8B, C, Sawaki et al., 2008; Sawaki et al., 2010).

In this study, our inferred seawater $^{87}Sr/^{86}Sr$ ratios from the Keping region decrease from ~0.7090 to ~0.7085 in the lower part of the Chigebrak Fm. with a slight rebound to more radiogenic values (~0.7091) at the top of this formation. This trend mimics the variation recorded in the terminal Proterozoic Dengying and Doushantuo Fm. on the South China Yangtze Platform (Sawaki et al., 2010). Sawaki et al. (2008) and Hohl et al. (2015a) reported increasing $^{87}Sr/^{86}Sr$ ratios in the upper Dengying Fm., coinciding the similar increasing trends recorded in the contemporarily deposited upper Chigebrak Fm. carbonates (Fig. 8). However, the magnitude of the total rise in $^{87}Sr/^{86}Sr$ ratios is smaller than those recorded by Sawaki et al. (2008) but comparable to that reported by Hohl et al. (2015a). This may be explained with erosion and denudation of the uppermost Chigebrak carbonate platform (He et al., 2018) and the incomplete outcrop situation at the Xiaofenghe section in South China (Hohl et al., 2015a). As a summary from the above discussion, we consider the Chigebrak Fm. to be equivalent to the Dengying Fm., revealing consistent Sr and C isotope stratigraphy (Fig. 7).

As discussed above, the scattering $^{87}Sr/^{86}Sr$ ratios obtained in carbonates from the Yurtus Fm. are likely results of restricted-basin seawater mixed with carbonate weathering fluid

(section 5.1.3, Fig. 6A, 6B and 6C) and thus may not be compared to the global seawater $^{87}Sr/^{86}Sr$ curve. We, therefore, exclude these data points from our Sr isotope composition curve as they may represent a restricted-basin signal (Bai et al., 2019; Yao et al., 2017) that is unsuitable for global correlations.

From the bottom of the Xiaoerbrak Fm. to the bottom of Shayilik Fm., the obtained $^{87}Sr/^{86}Sr$ ratios in carbonate leachates rise from ~0.7087 to ~0.7090, consistent with the reported seawater $^{87}Sr/^{86}Sr$ evolutionary curve during the Cambrian Series 2 (Montañez and Banner, 2000; Ebneth et al., 2001; Peng et al., 2012; Zhu et al., 2019) (Fig. 8). At the bottom of the Shayilik Fm., the $^{87}Sr/^{87}Sr$ ratios in the carbonates leachates decrease from ~0.7090 to ~0.7087, analogous to the global seawater $^{87}Sr/^{86}Sr$ curve at the Stage 4/Wuliuan Stage boundary (Peng et al., 2012; Zhu et al., 2019) (Fig. 8). Subsequently, $^{87}Sr/^{87}Sr$ ratios increase again at the middle part of the Shayilik Fm. and reach a peak of ~0.7092 in the middle part of the Awatagh Fm., coinciding the starting point of the $\delta^{13}C$ positive excursion "G" (Fig. 7). The SPICE and the maximum $^{87}Sr/^{87}Sr$ peak at around ~0.7092 characterize the boundary between the Guzhuangian and Paibian Stage (Montañez and Banner, 2000; Ebneth et al., 2001; Kouchinsky et al., 2008; Fan et al., 2011). As we inferred hereinbefore, based on the coincidence between the $^{87}Sr/^{87}Sr$ peak and the $\delta^{13}C$ positive excursion "G", this study correlates the middle-upper part of the Awatagh Fm. approximately to the boundary between the Guzhuangian and Paibian Stage. Apart from only one outlier with a much lower $^{87}Sr/^{86}Sr$ value (~0.7086) in the lower part of Xiaqiulitagh Fm., the $^{87}Sr/^{86}Sr$ ratios slowly decrease from ~0.7092 to ~0.7091 from the middle part of the Awatagh Fm. to the Xiaqiulitagh Fm., which are broadly similar to those ratios reported by Ebneth et al. (2001) and Montañez and Banner (2000).

In this study, as a whole, the $^{87}Sr/^{86}Sr$ ratios and the C isotope variations obtained in carbonates from two sections of the Keping region spanning the late-Ediacaran to the late-Cambrian show global consistency (Fig. 7 and Fig. 8), except those analyses performed in presumably diagenetically altered Sugetbrak Fm. and the Yurtus Fm. carbonates. Our results from the stratigraphic correlation between the Keping area and other parts of the world from the late-Ediacaran to the late-Cambrian are as follows:

i. The Chigebrak Fm. is presumably equivalent to the Dengying Fm. of the South China

623 Yangtze Platform.

624 **ii**. The base of the Xiaoerbrak Fm., which contains *Shizhudiscus* fossils, is slightly
625 stratigraphically higher than the base of the Cambrian Stage 3.

626 **iii**. The most negative $\delta^{13}C$ excursion "F" together with a decrease in $^{87}Sr/^{86}Sr$ characterize
627 the bottom of the Shayilik Fm., which can be regarded as the boundary between the Cambrian
628 Stage 4 and Cambrian Wuliuan in the Tarim Basin. This stratigraphic correlation is consistent
629 with the existing paleontological constraints in the Tarim Basin (Peng, 2009).

630 **iv.** The carbonate samples of the upper-middle part of the Awatagh Fm. archive a positive
631 $\delta^{13}C$ excursion "G" (likely equivalent to SPICE) and a peak value of $^{87}Sr/^{86}Sr$ ratios at ~0.7092,
632 presumably marking the base of the Cambrian Paibian Stage.

633

634 **5.4 Paleoenvironmental implications for the Tarim Basin at the PC/C**

635

636 Overall, the obtained seawater $^{87}Sr/^{86}Sr$ ratios in carbonates from this study and those
637 recorded in numerous carbonate successions from different paleo-continents show a stepwise
638 increase from late Ediacaran to late Cambrian (Furongian) which is superimposed by several
639 minor declines (Fig. 8 and Fig. 9). Meanwhile, the obtained $\delta^{13}C$ values in our study show four
640 prominent negative and three positive excursions that are identical to trends found in various
641 carbonate-based C isotope records at a global scale (Fig. 9).

642

643 **5.4.1 Late Ediacaran paleoenvironmental reconstruction of the Tarim Basin**

644

645 The integrated global carbonate $\delta^{13}C$ trend of late Ediacaran sections (Fig. 7) suggests that
646 the carbonate $\delta^{13}C$ record from the Keping region probably archives a primary global seawater
647 $\delta^{13}C$ signal during this interval. According to our C and Sr isotope stratigraphic correlation (Fig.
648 7 and Fig. 8), the lower part of the positive $\delta^{13}C$ excursion "A" in this study probably
649 corresponds to the uppermost Doushantuo negative $\delta^{13}C$ excursion which ended at around
650 551 Ma (Zhu et al., 2007). It is controversial whether DOUNCE/Shuram-Wonoka is
651 representative of the primary coeval seawater chemistry or not. Some researchers explained
652 the extreme negative $\delta^{13}C$ values of the DOUNCE/Shuram-Wonoka event by global changes in

653 the C isotopic composition of Ediacaran seawater as a result of the remineralization of a vast
654 dissolved organic carbon reservoir (cf. Rothman et al., 2003; Fike et al., 2006). Others
655 suggested a large flux of methane released from the seafloor (Bjerrum and Canfield, 2011) as
656 the cause, while Derry (2010) argued for a large-scale post-depositional diagenetic alteration.
657 In this study, samples from the Sugetbrak Fm., which constitute for the most of the lower
658 part of the positive excursion "A", exhibit a strong positive correlation in the $\delta^{13}C$-$\delta^{18}O$ plot (Fig.
659 5A) and negative correlations in the $^{87}Sr/^{86}Sr$-$\delta^{13}C$, $^{87}Sr/^{86}Sr$-$\delta^{18}O$ plots (Fig. 6H, 6I) in the
660 Sugetbrak Fm. and the correlations support a severe diagenetic alteration imprint. $^{87}Sr/^{86}Sr$
661 data of the diagenetically altered samples of this study is also comparable to the altered
662 samples in the Doushantuo Fm. from South China (Sawaki et al., 2010) (Fig. 8). However,
663 although this diagenetic alteration may relate to Derry's large-scale or even global post-
664 depositional diagenetic $\delta^{13}C$ variation hypothesis (Derry, 2010), it requires further diagenesis
665 evaluation by other proxies at a global scale (e.g. lithological evidence of widespread
666 deposition of authigenic carbonate).
667 Immediately above the altered samples from the Sugetbrak Fm., samples from the base
668 of the Chigebrak Fm. delineate the peak of the positive $\delta^{13}C$ excursion "A" and its recovery
669 towards lower values. Wood et al. (2015) also reported a positive $\delta^{13}C$ excursion (ca. 548 Ma,
670 equivalent to the excursion "A") in the carbonates of the Nama group from Namibia postdating
671 the appearance of calcified metazoans. The steep increase of calcified metazoans in the total
672 primary production could have amplified organic carbon burial and led to a net drawdown of
673 atmospheric CO_2, ultimately shifting the seawater $\delta^{13}C$ to more positive values (Knoll et al.,
674 1996). In this study, the positive $\delta^{13}C$ excursion "A" is accompanied by an $^{87}Sr/^{86}Sr$ decrease,
675 coinciding a lithological transition from more siliciclastic carbonates to micritic carbonates (Fig.
676 9) that may relate to a transgression event (Deng et al., 2019). Therefore, the recorded $^{87}Sr/^{86}Sr$
677 decrease in carbonates may imply suppressed continental silicate weathering due to reduced
678 continental silicates being exposed to physical-chemical weathering on land (Jiang et al., 2007)
679 and possible associated atmospheric CO_2 drawdown (Knoll et al., 1996).
680 Carbonates deposited in the Keping region above the positive excursion "A" show a
681 negative $\delta^{13}C$ excursion "B" accompanied by a decrease in seawater $^{87}Sr/^{86}Sr$ ratios (Fig. 9),
682 which was also reported in North India (Fig. 7, Jiang et al., 2007; Kaufman et al., 2006). The

683 further decrease in seawater $^{87}Sr/^{86}Sr$ might result from continued continental flooding and
684 suppressed continental weathering. At the same time, the $\delta^{13}C$ negative excursion "B" could
685 be explained by global ocean stratification by upwelling of deep-sea ^{13}C depleted suboxic to
686 euxinic waters in the terminal Proterozoic (cf. Jiang et al., 2007). Finally, the upper Chigebrak
687 Fm. carbonates record a rising seawater $^{87}Sr/^{86}Sr$ trend, consistent with the global seawater
688 record in the late Ediacaran pristine carbonate (Brasier et al., 1996; Sawaki et al., 2008),
689 possibly indicating enhanced silicate weathering as a result of increased silicates exposure
690 during large-scale regression (Brasier, 1996; Haq and Schutter, 2008).
691
692 **5.4.2 Terrenenvian Series and Cambrian Series 2 paleoenvironmental reconstruction of**
693 **the Tarim Basin**
694
695 As discussed in section 5.1.3, $^{87}Sr/^{86}Sr$ variations recorded in the Yurtus Fm. carbonates
696 are possibly caused by restricted basin seawater mixing with meteoric waters (Fig. 6). Further,
697 the widespread karst structures may represent a widely distributed hiatus between the
698 Chigebrak and Yurtus Fm. (Wu et al., 2018), which indicates a large scale sea-level drop during
699 the Ediacaran-Cambrian transition and is consistent with a proposed global sea-level shift
700 during this interval (Haq and Schutter, 2008; He et al., 2017). He et al. (2018) studied the
701 geographical distribution of the paleo-karst at the top of the Chigebrak Fm. and speculated
702 that there was an Ediacaran carbonate paleo-upland near to the Xiaoerbrak and Shiairik
703 sections during this time. Additionally, the paleo-karst structures in the uppermost of the
704 Chigebrak Fm. may indicate that meteoric fluids (with light O isotopic compositions) and
705 dissolution of Ediacaran carbonates (and their Sr isotope compositions) might have influenced
706 the Yurtus Fm. carbonate Sr isotope values.
707 The obtained $\delta^{13}C$ values in the Yurtus Fm. carbonates show no variation with $^{87}Sr/^{86}Sr$,
708 however, given the existence of a paleo-upland which might contribute to the "great
709 unconformity" at the PC/C boundary (He et al., 2017; He et al., 2018), the negative $\delta^{13}C$
710 excursions in the Yurtus Fm. may be a result of enhanced dissolved organic carbon (with low
711 $\delta^{13}C$ signals) remineralization as a result of oceanic ventilation during regression (He et al.,
712 2019).

During the Cambrian Series 2, the global seawater $^{87}Sr/^{86}Sr$ trend shows a slow rise from ~0.7087 to ~0.7090 (Kaufman et al., 1993; Derry et al., 1994; Montañez et al., 1996; Montañez and Banner, 2000; Ebneth et al., 2001, Fig. 8). This rise may record an increased radiogenic ^{87}Sr input from enhanced continental weathering. Further, increased weathering enhanced organic matter burial, and eventually caused the distinct positive $\delta^{13}C$ excursion "D". Finally, organic matter burial could have induced a net increase in oxygen in the deep waters (Guo et al., 2017) which potentially triggered the appearance of *Shizhudiscus* (Fig. 9, Qian and Xiao, 1984), that has higher oxygen demand for its cellular respiration and motile activities.

5.4.3 Causes of the ROECE event

The prominent global decrease in $^{87}Sr/^{86}Sr$ ratios at the boundary between the Cambrian Stage 4 and the Cambrian Wuliuan Stage is commonly explained by one of the following hypotheses:

i. Large-scale sea-level rise (Montañez and Banner, 2000; Hough et al., 2006). The flooding of continental areas decreases the input of radiogenic Sr to the oceans and therefore lower the $^{87}Sr/^{86}Sr$ ratios of seawater.

ii. Widespread rifting along with the Weddell Sea-South African sector of the paleo-Pacific margin of Laurentia (Curtis et al., 1999) exposes mafic rocks (enriched in ^{86}Sr) resulting in a net decrease in radiogenic Sr input.

Considering that the negative $\delta^{13}C$ excursion "F" obtained in the carbonates from the Keping region (down to ~-13 ‰) is much lower than -6 ‰, we rule out explanation "ii" as hydrothermal fluid CO_2 exhalation of mid-ocean ridge-type (with C isotope compositions usually > -6 ‰; Ishibashi et al., 1995) shows no such negative C isotope compositions. By contrast, the sea-level rise hypothesis represents a more plausible mechanism for the $^{87}Sr/^{86}Sr$ decrease in the contemporaneous seawater and is supported by the transgression event revealed in the sedimentary characteristics (Bai et al., 2019). Moreover, the extreme negative $\delta^{13}C$ recorded in the carbonates, which exceeds the magnitude of other ROECE-equivalent negative excursions in South China (Guo et al., 2010), can be hardly explained alone by a reduced dissolved inorganic carbon input into the ocean (Kump and Arthur, 1999). The

743 extreme negative $\delta^{13}C$ values observed in our studied carbonates are therefore probably
744 superimposed by an upwelling of ^{13}C-depleted deep-waters alongside the transgression,
745 leading to extreme low $\delta^{13}C$ values in the regional water-mass and the deposited carbonates
746 (Deng et al., 2019; Guo et al., 2017).
747
748 **5.4.4 Cambrian Series 3 (Miaolingian) and Furongian Series paleoenvironmental**
749 **reconstruction of the Tarim Basin**
750
751 During the Cambrian Series 3 (Miaolingian), the ambient seawater $^{87}Sr/^{86}Sr$ ratio increases
752 steadily to ~0.7092, while $\delta^{13}C$ values likewise rise to zero per mil succeeding the excursion "F"
753 (Fig. 9). Following Montañez and Banner (2000), this increase to more radiogenic seawater Sr
754 ratios may have resulted from orogenic events in Antarctica and Australia which is presumably
755 proximal to the Tarim Basin during the Miaolingian (Huang et al., 2000) as they exposed more
756 silicates on the continents prone to physicochemical weathering. This process may have
757 further enhanced the influx of key-nutrients (e.g. phosphorus) into the ocean (Montañez et
758 al., 1996), and ultimately leading to an amplification in the primary productivity and organic
759 carbon burial. As a result, the $\delta^{13}C$ values of co-precipitating carbonates from surface waters
760 could have increased towards higher values.
761 The beginning of the Furongian is characterized by a peak in both $\delta^{13}C$ and $^{87}Sr/^{86}Sr$ in
762 well-preserved carbonates (e.g. Montañez and Banner, 2000; Ebneth et al., 2001, Fig. 8). In
763 this study, contemporarily precipitated carbonates from the Tarim Basin yield $^{87}Sr/^{86}Sr$ ratios
764 between 0.7092 to 0.7091, which are close to modern seawater Sr isotope compositions (i.e.
765 present seawater $^{87}Sr/^{86}Sr$: 0.70916 (Ebneth et al., 2001)) and may imply a contribution from
766 a more radiogenic Sr-bearing rocks during the denudation of Damara Belt as part of the Pan-
767 African orogeny (Montañez and Banner, 2000; Ebneth et al., 2001). Moreover, a slight decrease
768 in the $^{87}Sr/^{86}Sr$ towards the end of the Furongian in the Keping region as well as in the global
769 record may imply the waning of the Pan-African orogeny (Fig. 9).
770
771 **6. Conclusions**
772

This study presents an integrated C and Sr isotope stratigraphic framework from late Ediacaran (ca. 551 Ma) to late Cambrian (< ca. 497 Ma) fully marine strata from the Keping region in the Tarim Basin, North-West China. The C and Sr isotope curves obtained from well-preserved carbonates are similar in their overall trends to those obtained in sections from other carbonate platforms worldwide. A chemo-stratigraphic correlation of our C and Sr isotope curves with globally reported isotope curves from various PC/C sections provides a stratigraphic framework for the late Ediacaran-late Cambrian strata in the Keping area, NW Tarim Basin. Furthermore, the obtained curves may contribute to the global seawater $\delta^{13}C$ and $^{87}Sr/^{86}Sr$ evolution curves and provide a reference for future stratigraphic correlations in the Tarim Basin and elsewhere.

Finally, our paleoenvironmental reconstruction shows bio-geochemical variations of the Tarim Basin seawater that were presumably governed by fluctuations in the hinterland weathering regime and temporal changes in the connection to the open ocean. The studied carbonates record both local as well as global seawater level changes, which may have controlled the influx of radiogenic Sr and key nutrients, restricting primary production, into the Tarim Basin. These cause-effect relationships provided in this study may have ultimately impacted the extent of organic C burial and the rapid diversification of metazoans.

Acknowledgements

The authors appreciate Rui Ding and Pufan Wang's assistance in the field and Huanling Lei and Jin Wang's help in the ultra-clean laboratory. The National Science and Technology Major Project of China (No. 2016ZX05004-004) and the Strategic Priority Research Program (B) of the Chinese Academy of Sciences (CAS) (XDB26000000) financially supported this study. Simon Hohl and Tianchen He were supported by the National Natural Science Foundation of China (funding Nos: 41650110480, 41750410690 and 41888101). Further Tianchen He was funded by the State Key Laboratory of Palaeobiology and Stratigraphy & Center for Excellence in Life and Paleoenvironment (Nanjing Institute of Geology and Palaeontology) (No.2018KF03).

References

Bai, Y., Xu, A., Liu, W., Zhao, Z. and Luo, P. (2019) Sedimentary characteristics of Lower and Middle Cambrian diamict in the northwestern Tarim Basin (in Chinese with English abstract). Natural Gas Industry 39, 46-57.

Banner, J.L. and Kaufman, J. (1994) The isotopic record of ocean chemistry and diagenesis preserved in non-luminescent brachiopods from Mississippian carbonate rocks, Illinois and Missouri. Geological Society of America Bulletin 106, 1074-1082.

Bjerrum, C.J. and Canfield, D.E. (2011) Towards a quantitative understanding of the late Neoproterozoic carbon cycle. Proceedings of the National Academy of Sciences 108, 5542-5547.

Brasier, M.D. (1996) The Basal Cambrian Transition and Cambrian Bio-Events (from Terminal Proterozoic Extinctions to Cambrian Biomeres), Global events and event stratigraphy in the Phanerozoic. Springer, Verlag Berlin Heidelberg.

Brasier, M.D., Shields, G., Kuleshov, V.N. and Zhegallo, E.A. (1996) Integrated chemo- and biostratigraphic calibration of early animal evolution: Neoproterozoic–early Cambrian of southwest Mongolia. Geological Magazine 133.

Burke, W.H., Denison, R.E., Hetherington, E.A., Koepnick, R.B., Nelson, H.F. and Otto, J.B. (1982) Variation of seawater $^{87}Sr/^{86}Sr$ throughout Phanerozoic time. Geology 10.

Chen, Y., Jiang, S., Zhou, X., Yang, W. and Han, L. (2010) $\delta^{30}Si$, $\delta^{18}O$ and elements geochemistry on the bedded siliceous rocks and cherts in dolostones from Cambrian strata, Tarim Basin (in Chinese with English abstract). Geochimica 39, 159-170.

Conway-Morris, S. (2003) The Cambrian “explosion” of metazoans and molecular biology: would Darwin be satisfied? International Journal of Developmental Biology 47, 505-515.

Cowie, G.L., Hedges, J.I., Prahl, F.G. and Delange, G.J. (1995) Elemental and Major Biochemical-Changes across on Oxidation Front in a Relict Turbidite - an Oxygen Effect. Geochimica Et Cosmochimica Acta 59, 33-46.

Cowie, J.W. and Glaessner, M.F. (1975) The Precambrian-Cambrian Boundary: A Symposium. Earth-Science Reviews 11, 209-251.

Craig, H. (1953) The geochemistry of the stable carbon isotopes. Geochimica Et Cosmochimica Acta 3, 53-92.

833 Curtis, M.L., Leat, P.T., R., R.T., Storey, B.C., Millar, I.L. and Randall, D.E. (1999) Middle Cambrian
834 rift-related volcanism in the Ellsworth Mountains, Antarctica-Tectonic implications for the
835 palaeo-Pacific margin of Gondwana. Tectonophysics 304, 275-299.
836 Deng, H., Tian, J., Zhang, X., Meng, W., Su, B., Yang, P. and Zeng, J. (2019) Sedimentary facies
837 characteristics and sedimentary patterns of Sinian in Akesu Area on the northwest margin
838 of Tarim Basin (In Chinese with English abstract). Journal of Northeast Petroleum
839 University 43, 20-32.
840 Denison, R.E., Koepnick, R.B., Burke, W.H. and Hetherington, E.A. (1998) Construction of the
841 Cambrian and Ordovician seawater $^{87}Sr/^{86}Sr$ curve. Chemical Geology 152, 325-340.
842 Depaolo, D.J. and Ingram, B.L. (1985) High-resolution stratigraphy with strontium isotopes.
843 Science 227, 938-941.
844 Derry, L.A. (2010) On the significance of $\delta^{13}C$ correlations in ancient sediments. Earth and
845 Planetary Science Letters 296, 497-501.
846 Derry, L.A., Brasier, M.D., Corfield, R.M., Rozanov, A.Y. and Zhuravlev, A.Y. (1994) Sr and C
847 isotopes in Lower Cambrian carbonates from the Siberian craton: A paleoenvironmental
848 record during the 'Cambrian explosion'. Earth and Planetary Science Letters 128, 671-681.
849 Ebneth, S., Shields, G.A., Veizer, J., Miller, J.F. and Shergold, J.H. (2001) High-resolution
850 strontium isotope stratigraphy across the Cambrian-Ordovician transition. Geochimica et
851 Cosmochimica Acta 65, 2273-2292.
852 Fan, R., Deng, S.H. and Zhang, X.L. (2011) Significant carbon isotope excursions in the Cambrian
853 and their implications for global correlations. Science China-Earth Sciences 54, 1686-1695.
854 Fike, D.A., Grotzinger, J.P., Pratt, L.M. and Summons, R.E. (2006) Oxidation of the Ediacaran
855 ocean. Nature 444, 744-747.
856 Geyer, G. and Landing, E. (2017) The Precambrian–Phanerozoic and Ediacaran–Cambrian
857 boundaries: a historical approach to a dilemma. Geological Society, London, Special
858 Publications 448, 311-349.
859 Guo, Q., Deng, Y., Hu, J. and Wang, L. (2017) Carbonate carbon isotope evolution of seawater
860 across the Ediacaran–Cambrian transition: evidence from the Keping area, Tarim Basin,
861 NW China. Geological Magazine 154, 1244-1256.
862 Guo, Q., Strauss, H., Liu, C., Zhao, Y., Yang, X., Peng, J. and Yang, H. (2010) A negative carbon

isotope excursion defines the boundary from Cambrian Series 2 to Cambrian Series 3 on the Yangtze Platform, South China. Palaeogeography, Palaeoclimatology, Palaeoecology 285, 143-151.

Haq, B.U. and Schutter, S.R. (2008) A chronology of Paleozoic sea-level changes. Science 322, 64-68.

He, J., Qing, H. and Xu, B. (2018) The unconformity-related palaeokarst in the uppermost Ediacaran carbonate rocks in the northwestern Tarim Block, NW China: implication for sedimentary evolution during the Ediacaran–Cambrian transition. International Geology Review 61, 839-852.

He, T., Zhou, Y., Vermeesch, P., Rittner, M., Miao, L., Zhu, M., Carter, A., Strandmann, P.A.E.P.v. and Shields, G.A. (2017) Measuring the 'Great Unconformity' on the North China Craton using new detrital zircon age data. Geological Society of London Special Publications 448, 145-159.

He, T., Zhu, M., Mills, B.J.W., Wynn, P.M., Zhuravlev, A.Y., Tostevin, R., Pogge von Strandmann, P.A.E., Yang, A., Poulton, S.W. and Shields, G.A. (2019) Possible links between extreme oxygen perturbations and the Cambrian radiation of animals. Nature Geoscience 12, 468-474.

He, X., Xu, B. and Yuan, Z. (2007) C-isotope composition and correlation of the Upper Neoproterozoic in Keping area, Xinjiang. Chinese Science Bulletin 52, 504-511.

Hohl, S.V., Becker, H., Gamper, A., Jiang, S.-Y., Wiechert, U., Yang, J.-H. and Wei, H.-Z. (2015a) Secular changes of water chemistry in shallow-water Ediacaran ocean: Evidence from carbonates at Xiaofenghe, Three Gorges area, Yangtze Platform, South China. Precambrian Research 270, 50-79.

Hohl, S.V., Becker, H., Herzlieb, S. and Guo, Q. (2015b) Multiproxy constraints on alteration and primary compositions of Ediacaran deep-water carbonate rocks, Yangtze Platform, South China. Geochimica Et Cosmochimica Acta 163, 262-278.

Hohl, S.V., Becker, H., Jiang, S.-Y., Ling, H.-F., Guo, Q. and Struck, U. (2017) Geochemistry of Ediacaran cap dolostones across the Yangtze Platform, South China: implications for diagenetic modification and seawater chemistry in the aftermath of the Marinoan glaciation. Journal of the Geological Society 174, 893-912.

Hough, M.L., Shields, G.A., Evins, L.Z., Strauss, H., Henderson, R.A. and Mackenzie, S. (2006) A significant sulphur isotope event at c. 510 Ma: a possible anoxia-extinction-volcanism connection during the Early-Middle Cambrian transition? Terra Nova 18, 257-263.

Huang, B., Zhu, R., Otofuji, Y. and Yang, Z. (2000) The Early Paleozoic paleogeography of the North China block and the other major blocks of China. Chinese Science Bulletin 45, 1057-1065.

Ishibashi, J., Sano, Y., Wakita, H., Gamo, T., Tsutsumi, M. and Sakai, H. (1995) Helium and Carbon geochemistry of hydrothermal fluids from the Mid-Okinawa trough Back-Arc Basin, southwest of Japan. Chemical Geology 123, 1-15.

Ishikawa, T., Ueno, Y., Komiya, T., Sawaki, Y., Han, J., Shu, D., Li, Y., Maruyama, S. and Yoshida, N. (2008) Carbon isotope chemostratigraphy of a Precambrian/Cambrian boundary section in the Three Gorge area, South China: Prominent global-scale isotope excursions just before the Cambrian Explosion. Gondwana Research 14, 193-208.

Jacobsen, S.B. and Kaufman, A.J. (1999) The Sr, C and O isotopic evolution of Neoproterozoic seawater. Chemical Geology 161, 37-57.

Jiang, G., Kaufman, A.J., Christie-Blick, N., Zhang, S. and Wu, H. (2007) Carbon isotope variability across the Ediacaran Yangtze platform in South China: Implications for a large surface-to-deep ocean $\delta^{13}C$ gradient. Earth and Planetary Science Letters 261, 303-320.

Jones, C.E., Jenkyns, H.C., Coe, A.L. and Hesselbo, S.P. (1994) Strontium isotopic variations in Jurassic and Cretaceous seawater. Geochimica et Cosmochimica Acta 58, 3061-3074.

Kaufman, A.J., Jacobsen, S.B. and Knoll, A.H. (1993) The Vendian record of Sr and C isotopic variations in seawater: Implications for tectonics and paleoclimate. Earth and Planetary Science Letters 120, 409-430.

Kaufman, A.J., Jiang, G., Christie-Blick, N., Banerjee, D.M. and Rai, V. (2006) Stable isotope record of the terminal Neoproterozoic Krol platform in the Lesser Himalayas of northern India. Precambrian Research 147, 156-185.

Kaufman, A.J. and Knoll, A.H. (1995) Neoproterozoic variations in the C-isotopic composition of seawater: stratigraphic and biogeochemical implications. Precambrian Research 73, 27-49.

Keto, L.S. and Jacobsen, S.B. (1987) Nd and Sr Isotopic Variations of Early Paleozoic Oceans.

923 Earth and Planetary Science Letters 84, 27-41.
924 Knoll, A.H., Bambach, R.K., Canfield, D.E. and Grotzinger, J.P. (1996) Comparative earth history
925 and Late Permian mass extinction. Science 273, 452-457.
926 Kouchinsky, A., Bengtson, S., Gallet, Y., Korovnikov, I., Pavlov, V., Runnegar, B., Shields, G., Veizer,
927 J.A.N., Young, E. and Ziegler, K. (2008) The SPICE carbon isotope excursion in Siberia: a
928 combined study of the upper Middle Cambrian–lowermost Ordovician Kulyumbe River
929 section, northwestern Siberian Platform. Geological Magazine 145.
930 Kouchinsky, A., Bengtson, S., Runnegar, B., Skovsted, C., Steiner, M. and Vendrasco, M. (2011)
931 Chronology of early Cambrian biomineralization. Geological Magazine 149, 221-251.
932 Kump, L.R. and Arthur, M.A. (1999) Interpreting carbon-isotope excursions: carbonates and
933 organic matter. Chemical Geology 161, 181-198.
934 Landing, E. (1989) Paleoecology and distribution of the Early Cambrian rostroconch Watsonella
935 crosbyi Grabau. Journal of Paleontology 63, 566-573.
936 Li, D., Ling, H.-F., Shields-Zhou, G.A., Chen, X., Cremonese, L., Och, L., Thirlwall, M. and Manning,
937 C.J. (2013) Carbon and strontium isotope evolution of seawater across the Ediacaran–
938 Cambrian transition: Evidence from the Xiaotan section, NE Yunnan, South China.
939 Precambrian Research 225, 128-147.
940 Li, D., Shields-Zhou, G.A., Ling, H.-F. and Thirlwall, M. (2011) Dissolution methods for strontium
941 isotope stratigraphy: Guidelines for the use of bulk carbonate and phosphorite rocks.
942 Chemical Geology 290, 133-144.
943 Li, D., Zhang, X., Hu, D., Chen, X., Huang, W., Zhang, X., Li, M., Qin, L., Peng, S., Shen, Y. (2018)
944 Evidence of a large δ^{13}Ccarb and δ^{13}Corg depth gradient for deep-water anoxia during the
945 late Cambrian SPICE event. Geology 46, 631–634.
946 Maloof, A.C., Porter, S.M., Moore, J.L., Dudas, F.O., Bowring, S.A., Higgins, J.A., Fike, D.A. and
947 Eddy, M.P. (2010) The earliest Cambrian record of animals and ocean geochemical change.
948 Geological Society of America Bulletin 122, 1731-1774.
949 Marshall, J.D. (1992) Climatic and Oceanographic Isotopic Signals from the Carbonate Rock
950 Record and Their Preservation. Geological Magazine 129, 143-160.
951 McArthur, J.M., Howarth, R.J. and Shields, G.A. (2012) Strontium Isotope Stratigraphy, The
952 Geologic Time Scale, pp. 127-144.

McCrea, J.M. (1950) On the isotopic chemistry of carbonates and a paleotemperature scale. Journal of Chemical Physics 18, 849–857.

McKerrow, W.S., Scotese, C.R. and Brasier, M.D. (1992) Early Cambrian continental reconstructions. Journal of the Geological Society 149, 599-606.

Merdith, A.S., Collins, A.S., Williams, S.E., Pisarevsky, S., Foden, J.D., Archibald, D.B., Blades, M.L., Alessio, B.L., Armistead, S., Plavsa, D., Clark, C. and Müller, R.D. (2017) A full-plate global reconstruction of the Neoproterozoic. Gondwana Research 50, 84-134.

Melezhik, V.A., Pokrovsky, B.G., Fallick, A.E., Kuznetsov, A.B. and Bujakaite, M.I. (2009) Constraints on $^{87}Sr/^{86}Sr$ of Late Ediacaran seawater: insight from Siberian high-Sr limestones. Journal of the Geological Society 166, 183-191.

Montañez, I.P. and Banner, J.L. (2000) Evolution of the Sr and C Isotope Composition of Cambrian Oceans. GSA Today 10, 1-23.

Montañez, I.P., Banner, J.L., Osleger, D.A., Borg, L.E. and Bosserman, P.J. (1996) Integrated Sr isotope variations and sea-level history of Middle to Upper Cambrian platform carbonates: Implications for the evolution of Cambrian seawater $^{87}Sr/^{86}Sr$. Geology 24, 917-920.

Nier A. (1938) The Isotopic Constitution of Strontium, Barium, Bismuth, Thallium and Mercury. Physical Reviews 54, 275–278.

Ogg, J.G., Ogg, G.M. and Gradstein, F.M. (2016) A Concise Geologic Time Scale. Elsevier, Paris.

Palmer, M.R. and Edmond, J.M. (1989) The strontium isotope budget of the modern ocean. Earth and Planetary Science Letters 92, 11-26.

Peng, S., Babcock, L., Robison, R., Lin, H., Rees, M. and Saltzman, M. (2004) Global Standard Stratotype-section and Point (GSSP) of the Furongian Series and Paibian Stage (Cambrian). Lethaia 37, 365-379.

Peng, S., Babcock, L.E. and Cooper, R.A. (2012) The Cambrian Period, The Geologic Time Scale, pp. 437-488.

Peng, S.C. (2009) The newly-developed Cambrian biostratigraphic succession and chronostratigraphic scheme for South China. Chinese Science Bulletin 54, 4161-4170.

Qian, J. and Xiao, B. (1984) An Early Cambrian Small Shelly Fauna From Asku-Wushi Region, Xinjiang (in Chinese with English abstract). Professional Papers of Stratigraphy and Palaeontology 2, 65-90+166-169.

983 Qian, Y. and Bengtson, S. (1989) Palaeontology and biostratigraphy of the Early Cambrian
984 Meishucunian stage in Yunnan Province, South China. Universitetsforlaget, Oslo.
985 Qian, Y., Feng, W.-m., Li, G., Yang, A.-h., Feng, M., Zhao, X. and Xiao, B. (2009) Taxonomy and
986 biostratigraphy of the early Cambrian univalved mollusc fossils from Xinjiang. Acta
987 Micropalaeontologica Sinica 26, 193-210.
988 Qian, Y., Yin, G.-z. and Xiao, B. (2000) Opercula of Hyoliths and Operculum-like fossils from the
989 Lower Cambrian Yuertus Formation, Xinjiang (in Chinese with English abstract). Acta
990 Micropalaeontologica Sinica 17, 404-415.
991 Rothman, D.H., Hayes, J.M. and Summons, R.E. (2003) Dynamics of the Neoproterozoic carbon
992 cycle. Proceedings of the National Academy of Sciences 100, 8124-8129.
993 Saltzman, M.R., Runnegar, B. and Lohmann, K.C. (1998) Carbon isotope stratigraphy of Upper
994 Cambrian (Steptoean Stage) sequences of the eastern Great Basin: Record of a global
995 oceanographic event. Geological Society of America Bulletin 110, 285-297.
996 Sawaki, Y., Ohno, T., Fukushi, Y., Komiya, T., Ishikawa, T., Hirata, T. and Maruyama, S. (2008) Sr
997 isotope excursion across the Precambrian–Cambrian boundary in the Three Gorges area,
998 South China. Gondwana Research 14, 134-147.
999 Sawaki, Y., Ohno, T., Tahata, M., Komiya, T., Hirata, T., Maruyama, S., Windley, B.F., Han, J., Shu,
1000 D. and Li, Y. (2010) The Ediacaran radiogenic Sr isotope excursion in the Doushantuo
1001 Formation in the Three Gorges area, South China. Precambrian Research 176, 46-64.
1002 Shields-Zhou, G. and Zhu, M. (2013) Biogeochemical changes across the Ediacaran–Cambrian
1003 transition in South China. Precambrian Research 225, 1-6.
1004 Steiner, M., Li, G., Qian, Y. and Zhu, M. (2004) Lower Cambrian small shelly fossils of northern
1005 Sichuan and southern Shaanxi (China), and their biostratigraphic importance. Geobios 37,
1006 259-275.
1007 Sun, X.-l., Chen, J.-f., Zheng, J.-j. and Liu, W.-h. (2004) Geochemical characteristics of organic
1008 matter-rich sedimentary strata in Lower Cambrian, Tarim Basin and its origins. Acta
1009 Sedimentologica Sinica 22, 548-552.
1010 Thomas, W.A., Astini, R.A. and Denison, R.E. (2001) Strontium isotopes, age, and tectonic
1011 setting of Cambrian salinas along the rift and transform margins of the Argentine
1012 Precordillera and southern Laurentia. Journal of Geology 109, 231-246.

1013 Thomson, J., Jarvis, I., Green, D.R.H., Green, D.A. and Clayton, T. (1998) Mobility and immobility
1014 of redox-sensitive elements in deep-sea turbidites during shallow burial. Geochimica et
1015 Cosmochimica Acta 62, 643-656.
1016 Valentine, J.W., Jablonski, D. and Erwin, D.H. (1999) Fossils, molecules and embryos: new
1017 perspectives on the Cambrian explosion. Development 126, 851-859.
1018 Wang, W., Xiao, B., Zhang, S. and Zhu, Z. (1985) Division and correlation of Cambrian system in
1019 Aksu-Wushi district of Xinjiang (in Chinese with English abstract). Xinjiang Geology 3, 59-
1020 75.
1021 Wang, X., Hu, W., Li, Q. and Zhu, J. (2011a) Negative carbon isotope excursion on the Cambrian
1022 Series 2-Series 3 boundary for Penglaiba section in Tarim Basin and its significances (in
1023 Chinese with English Abstract). Geological Review 57, 17-23.
1024 Wang, X., Hu, W., Yao, S., Chen, Q. and Xie, X. (2011b) Carbon and strontium isotopes and
1025 global correlation of Cambrian Series 2-Series 3 carbonate rocks in the Keping area of the
1026 northwestern Tarim Basin, NW China. Marine and Petroleum Geology 28, 992-1002.
1027 Wang, Y., He, J., Wei, W. and Xu, B. (2010) Study on the Late Proterozoic sedimentary facies
1028 and sequence stratigraphy in Aksu area, Xinjiang (in Chinese with English abstract). Acta
1029 Petrologica Sinica 26, 2519-2528.
1030 Wood, R.A., Poulton, S.W., Prave, A.R., Hoffmann, K.H., Clarkson, M.O., Guilbaud, R., Lyne, J.W.,
1031 Tostevin, R., Bowyer, F., Penny, A.M., Curtis, A. and Kasemann, S.A. (2015) Dynamic redox
1032 conditions control late Ediacaran metazoan ecosystems in the Nama Group, Namibia.
1033 Precambrian Research 261, 252-271.
1034 Wotte, T., Strauss, H. and Sundberg, F.A. (2011) Carbon and sulfur isotopes from the Cambrian
1035 Series 2-Cambrian Series 3 of Laurentia and Siberia, in: Hollingsworth, J.S., Sundberg, F.A.,
1036 Foster, J.R. (Eds.), The 16th Field Conference Of The Cambrian Stage Subdivision Working
1037 Group International Subcommission On Cambrian Stratigraphy. Museum of Northern
1038 Arizona, Flagstaff, Arizona and Southern Nevada, United States, pp. 43-60.
1039 Wu, L., Guan, S., Zhang, S., Yang, H., Jin, J., Zhang, X. and Zhang, C. (2018) Neoproterozoic
1040 stratigraphic framework of the Tarim Craton in NW China: Implications for rift evolution.
1041 Journal of Asian Earth Sciences 158, 240-252.
1042 Xu, B., Zheng, H.F., Yao, H.T. and Li, Y.G. (2003) C-isotope composition and significance of the

1043 Sinian on the Tarim plate. Chinese Science Bulletin 48, 385-389.
1044 Xu, Z. and Han, G. (2009) Chemical and strontium isotope characterization of rainwater in
1045 Beijing, China. Atmospheric Environment 43, 1954-1961.
1046 Yang, B., Steiner, M., Li, G. and Keupp, H. (2014a) Terreneuvian small shelly faunas of East
1047 Yunnan (South China) and their biostratigraphic implications. Palaeogeography,
1048 Palaeoclimatology, Palaeoecology 398, 28-58.
1049 Yang, B., Zhang, L., Danelian, T., Feng, Q. and Steiner, M. (2014b) Chert-hosted small shelly
1050 fossils: expanded tool of biostratigraphy in the Early Cambrian. Gff 136, 303-308.
1051 Yao, C.Y., Ding, H.F., Ma, D.S. and Li, G.X. (2014) Carbon isotope features of the Sugetbrak
1052 section in the Aksu-Wushi Area, Northwest China: Implications for the
1053 Precambrian/Cambrian stratigraphic correlations. Acta Geologica Sinica-English Edition
1054 88, 1535-1546.
1055 Yao, C., Guo, W., Liu, J. and Li, H. (2017) Multiple Proxies on the Paleoenvironment of the Early
1056 Cambrian Marine Black Rock Series in the Tarim Basin, NW China: Molybdenum Isotope
1057 and Trace Element Evidence. International Journal of Geosciences 08, 965-983.
1058 Yu, B.-s., Chen, J., Li, X. and Lin, C. (2004) Rare earth and trace element patterns in bedded-
1059 cherts from the bottom of the Lower Cambrian in the Northern Tarim Basin, Northwest
1060 China: Implication for depositional environments (in Chinese with English abstract). Acta
1061 Sedimentologica Sinica 22, 547-552.
1062 Yu, B.S., Dong, H.L., Widom, E., Chen, J.Q. and Lin, C.S. (2009) Geochemistry of basal Cambrian
1063 black shales and cherts from the Northern Tarim Basin, Northwest China: Implications for
1064 depositional setting and tectonic history. Journal of Asian Earth Sciences 34, 418-436.
1065 Zhan, S., Chen, Y., Xu, B., Wang, B. and Faure, M. (2007) Late Neoproterozoic paleomagnetic
1066 results from the Sugetbrak Formation of the Aksu area, TarimBasin (NW China) and their
1067 implications to paleogeographic reconstructions and the snowball Earth hypothesis.
1068 Precambrian Research 154, 143-158.
1069 Zhou, C., Yuan, X., Xiao, S., Chen, Z. and Hua, H. (2018) Ediacaran integrative stratigraphy and
1070 timescale of China. Science China Earth Sciences.
1071 Zhou, X., Chen, D., Dong, S., Zhang, Y., Guo, Z., Wei, H. and Yu, H. (2015) Diagenetic barite
1072 deposits in the Yurtus Formation in Tarim Basin, NW China: Implications for barium and

sulfur cycling in the earliest Cambrian. Precambrian Research 263, 79-87.

Zhou, Y., Pogge von Strandmann, P.A.E., Zhu, M., Ling, H., Manning, C., Li, D., He, T., Shields, G.A. (2020) Reconstructing Tonian seawater $^{87}Sr/^{86}Sr$ using calcite microspar. Geology.

Zhou, Z. (2001) Stratigraphy of the Tarim Basin (in Chinese), 1 ed. Science Press, Beijing.

Zhou, Z. and Chen, P. (1990) Biostratigraphy and geological evolution of Tarim (in Chinese). Science Press, Beijing.

Zhu, M.-Y., Babcock, L.E. and Peng, S.-C. (2006) Advances in Cambrian stratigraphy and paleontology: Integrating correlation techniques, paleobiology, taphonomy and paleoenvironmental reconstruction. Palaeoworld 15, 217-222.

Zhu, M., Yang, A., Yuan, J., Li, G., Zhang, J., Zhao, F., Ahn, S.-Y. and Miao, L. (2019) Cambrian integrative stratigraphy and timescale of China. Science China Earth Sciences 62, 25-60.

Zhu, M., Zhang, J. and Yang, A. (2007) Integrated Ediacaran (Sinian) chronostratigraphy of South China. Palaeogeography, Palaeoclimatology, Palaeoecology 254, 7-61.

Figure captions:

Fig. 1 A) Paleogeographic maps of the Tarim Basin (yellow) and South China (orange) during the Ediacaran (A-1) and the middle Cambrian (A-2) (modified from Merdith et al., 2017), abbreviations: T for the Tarim Basin and SC for South China. B) Proterozoic and Phanerozoic geological units of the Keping region (red square on the inlet map B-1) with locations of the sections indicated by red stars (modified from Zhou et al., 2015).

Fig. 2 Comprehensive stratigraphic log of sections from the Keping region (Modified after Zhou and Chen, 1990; Zhou, 2001; Peng, 2009; Wang et al., 2011b). The markers in the "Sampling Location" column represent the heights/distances of samples (the height scale of 50 m can be found in the upper-right corner), the Ediacaran samples are from the Shiairik section (red dashes), and the Cambrian samples are from the Xiaoerbrak section (black dashes). The dotted lines represent less defined formation boundaries; the colored arrows mark the biozone and fossil occurrence range.

Fig. 3 Schematic flow diagram of the carbonate dissolution procedure.

Fig. 4 C, O and Sr isotopic isotope compositions obtained in carbonate leachates from the late Ediacaran to Cambrian at the studied sections in the Keping region. The green/orange fields represent positive/negative C isotope excursions, respectively. The inserted column shows the $\delta^{13}C$ variation in the Yurtus Fm. in 10-fold height magnification for better visibility.

Fig. 5 C, O isotope compositions and Mn/Sr ratios for the late-Ediacaran samples (A) and Cambrian samples (B). The yellow layer represents $\delta^{18}O < -10$ ‰.

Fig. 6 Sr isotopic composition vs. $\delta^{13}C$, $\delta^{18}O$, Sr concentration, Mn/Sr, Mg/Ca, carbonate content (%, = CaO (%) + MgO (%)) and [Rb] for the Cambrian samples (A-G) and late Ediacaran samples (H-N). For the fluid-carbonate mixing model in Yurtus Fm., a meteoric fluid composition of $^{87}Sr/^{86}Sr = 0.7085$, $\delta^{18}O = -14$, $\delta^{13}C = -5$ and Sr concentration of 600 ppm was chosen together with a presumed localized seawater of $^{87}Sr/^{86}Sr = 0.7102$, $\delta^{18}O = 0.5$, $\delta^{13}C = 0.5$, and Sr concentration of 50 ppm was used in the model.

Fig. 7 Comparison of $\delta^{13}C$ signatures recorded in carbonate rocks spanning late-Ediacaran to late-Cambrian strata in A) the Tarim Basin (this study), B) the presumable global Cambrian seawater standard $\delta^{13}C$ variations, mainly derived from South China (Zhu et al., 2019), C-D-G-I) South China (Jiang et al., 2007; Guo et al., 2010; Li et al., 2013), H) South-western Mongolia

(Brasier et al., 1996) E) Laurentia (Montañez and Banner, 2000), F) Siberia (Wotte et al., 2011) and J) North India (Kaufman et al., 2006). Red dots represent screened samples with severe diagenetic alteration; the dotted line indicates uncertain boundaries; the red line indicates the first appearance of trilobites. Paleontological data are derived from Qian and Xiao (1984); Qian and Bengtson (1989); Peng (2009); Wang et al. (2011b). The age of the beginning of the Paibian stage is set to 497 Ma (Ogg et al., 2016).

Fig. 8 Comparison of $^{87}Sr/^{86}Sr$ ratios from the late-Ediacaran to the late-Cambrian in A) Cambrian global seawater $^{87}Sr/^{86}Sr$ standard proposed by Peng et al. (2012); Zhu et al. (2019); of which data is derived from Derry et al. (1994); Montañez and Banner (2000); Ebneth et al. (2001); Kouchinsky et al. (2008); dotted lines represent less defined formation boundaries, B) & C) Sr isotope data from the Yangtze Platform, South China (Sawaki et al., 2008; Sawaki et al., 2010) and D) Keping Area, NW Tarim Basin (this study) where the data from the altered carbonates from the Yurtus and Sugetbrak Fm. is excluded.

Fig. 9 C and Sr isotope evolution of seawater in the Keping region, NW Tarim. This figure includes the stratigraphic correlation and supposed age constraints. Colored (green/orange) rectangular boxes represent the durations of the $\delta^{13}C$ excursions. Colored arrows pointed out the occurrences of the fossil-bearing strata; red dots indicate diagenetically altered $^{87}Sr/^{86}Sr$ values and the diagenetically altered $^{87}Sr/^{86}Sr$ values from the Yurtus and Sugetbrak carbonates are excluded in this figure.

1137 **Table 1.** Analytical results of C, O, Sr isotope compositions and Ca, Mg, Mn, Sr, Rb concentrations of samples from the Keping area, NW Tarim Basin, NW China.

Sample	Formation	Lithology	Height (m)	$\delta^{13}C$ (V-PDB, ‰)	$\delta^{18}O$ (V-PDB, ‰)	$^{87}Sr/^{86}Sr$	±σ	Ca (%)	Mg (%)	Mn (ppm)	Rb (ppm)	Sr (ppm)	Mn/Sr	Mg/Ca	$^{85}Rb/^{86}Sr$
SARK-1	Sugetbrak	limestone	-217.9	-5.49	-9.88	0.709471	0.000005	32.4	0.52	2180	1.56	700	3.11	0.02	0.000341
SARK-2	Sugetbrak	limestone	-215.0	-4.68	-9.44					2340	1.94	590	3.96		
SARK-3	Sugetbrak	dolostone	-156.2	1.00	-5.90	0.709365	0.000005	19.7	6.42	781	1.29	171	4.57	0.33	0.001164
SARK-4	Sugetbrak	dolostone	-153.0	3.67	-4.20					436	0.83	160	2.73		
SARK-5	Sugetbrak	dolostone	-151.4	3.90	-3.96					700	4.17	148	4.72		
SARK-6	Sugetbrak	dolostone	-150.5	4.14	-1.83					642	2.13	62.1	10.3		
SARK-7	Sugetbrak	dolostone	-148.5	4.67	-2.53	0.709158	0.000004	13.4	7.39	669	1.60	147	4.55	0.55	0.000280
SARK-8	Sugetbrak	dolostone	-146.0	5.60	-0.85					488	1.06	175	2.78		
SARK-9	Chigebrak	dolostone	-143.0	6.37	-3.02	0.708849	0.000005	15.3	8.64	219	0.69	235	0.93	0.57	0.000458
SARK-10	Chigebrak	dolostone	-142.1	6.61	-3.56					277	0.65	171	1.62		
SARK-11	Chigebrak	dolostone	-141.0	6.56	-3.49	0.709069	0.000005	12.2	6.71	369	1.46	253	1.46	0.55	0.000726
SARK-12	Chigebrak	dolostone	-140.0	6.96	-0.98					205	0.69	201	1.02		
SARK-13	Chigebrak	dolostone	-138.0	7.94	-2.50					182	0.81	227	0.80		
SARK-14	Chigebrak	dolostone	-135.0	5.59	-5.32	0.708934	0.000005	16.3	9.12	499	1.31	141	3.54	0.56	0.001235
SARK-15	Chigebrak	dolostone	-133.5	5.01	-2.41					312	1.23	180	1.73		
SARK-16	Chigebrak	dolostone	-132.0	5.68	-2.78					241	0.57	174	1.38		
SARK-17	Chigebrak	dolostone	-130.5	5.54	-2.60	0.708962	0.000006	15.7	9.16	259	0.74	171	1.51	0.58	0.000738
SARK-18	Chigebrak	dolostone	-129.6	5.93	-2.63					363	1.16	207	1.76		
SARK-19	Chigebrak	dolostone	-129.0	5.69	-2.36					243	0.62	203	1.20		
SARK-20	Chigebrak	dolostone	-127.0	4.87	-3.65	0.708994	0.000005	13.4	7.83	402	1.67	226	1.78	0.58	0.000579
SARK-21	Chigebrak	dolostone	-125.2	5.88	-2.16					279	0.65	180	1.55		
SARK-22	Chigebrak	dolostone	-124.2	5.93	-2.58					218	0.78	176	1.24		
SARK-23	Chigebrak	dolostone	-122.0	4.41	-0.72	0.708806	0.000005	12.6	7.27	410	1.23	191	2.15	0.58	0.000467
SARK-24	Chigebrak	dolostone	-119.0	4.40	-2.30					297	1.42	115	2.58		
SARK-25	Chigebrak	dolostone	-117.2	4.12	0.15					222	0.77	142	1.56		

Sample	Formation	Lithology	Height (m)	$\delta^{13}C$ (V-PDB, ‰)	$\delta^{18}O$ (V-PDB, ‰)	$^{87}Sr/^{86}Sr$	±σ	Ca (%)	Mg (%)	Mn (ppm)	Rb (ppm)	Sr (ppm)	Mn/Sr	Mg/Ca	$^{85}Rb/^{86}Sr$
SARK-26	Chigebrak	dolostone	-114.0	3.50	-2.80	0.708816	0.000004	17.5	10.1	190	0.69	158	1.20	0.58	0.000260
SARK-27	Chigebrak	dolostone	-111.0	3.63	-2.47					156	0.72	220	0.71		
SARK-28	Chigebrak	dolostone	-109.0	2.06	-3.56					152	0.54	170	0.89		
SARK-29	Chigebrak	dolostone	-107.0	0.97	-3.10	0.708750	0.000005	16.8	9.80	149	0.54	169	0.88	0.58	0.000474
SARK-30	Chigebrak	dolostone	-100.3	1.70	-2.87	0.708611	0.000005	18.9	11.1	207	0.51	104	1.99	0.59	0.000455
SARK-31	Chigebrak	dolostone	-99.6	1.69	-2.98					18.7	0.45				
SARK-32	Chigebrak	dolostone	-98.0	2.35	-3.11					199	0.50	161	1.23		
SARK-33	Chigebrak	dolostone	-95.0	2.57	-3.12					108	0.96	73.5	1.47		
SARK-34	Chigebrak	dolostone	-90.0	2.05	-5.08	0.708746	0.000005	17.9	10.1	396	0.68	127	3.11	0.57	0.000641
SARK-35	Chigebrak	dolostone	-86.0	2.13	-5.16					464	0.47	144	3.23		
SARK-36	Chigebrak	dolostone	-83.0	2.52	-1.52					256	0.44	130	1.96		
SARK-37	Chigebrak	dolostone	-80.0	3.17	-2.45					165	0.44	123	1.34		
SARK-38	Chigebrak	dolostone	-75.0	3.05	-1.04	0.708464	0.000005	19.8	11.5	173	0.44	138	1.25	0.58	0.000689
SARK-39	Chigebrak	dolostone	-66.0	2.70	-2.10					179	0.43	163	1.10		
SARK-40	Chigebrak	dolostone	-60.0	2.75	-0.10					177	0.47	440	0.40		
SARK-41	Chigebrak	dolostone	-56.0	2.86	-0.05	0.708544	0.000005	19	11.0	229	0.50	125	1.83	0.58	0.000469
SARK-42	Chigebrak	dolostone	-53.0	3.22	0.42					110	0.45	107	1.03		
SARK-43	Chigebrak	dolostone	-48.2	2.88	-1.91					136	0.61	78.8	1.73		
SARK-44	Chigebrak	dolostone	-45.0	2.98	-0.91	0.708775	0.000005	18.2	10.5	155	0.61	116	1.33	0.58	0.001286
SARK-45	Chigebrak	dolostone	-40.0	2.75	-1.78					185	0.59	104	1.78		
SARK-46	Chigebrak	dolostone	-34.5	2.33	-3.92					336	0.55	94.2	3.57		
SARK-47	Chigebrak	dolostone	-6.0	1.97	-5.54	0.708880	0.000005	13.3	7.70	557	0.94	143	3.90	0.58	0.000579
SARK-48	Chigebrak	dolostone	-3.0	1.65	-6.49	0.709089	0.000004	14.6	8.20	604	1.98	208	2.91	0.56	0.000610
SARK-49	Chigebrak	dolostone	-2.0	1.98	-5.97					546	0.92	167	3.26		
XBK-1	Yurtus	phosphorite	0.5							1988	1.31	386	5.15		
XBK-2	Yurtus	phosphorite	2.5			0.709950	0.000008	1.04	0.19	0.36	0.25	58.4	0.01	0.18	0.000483

Sample	Formation	Lithology	Height (m)	$\delta^{13}C$ (V-PDB, ‰)	$\delta^{18}O$ (V-PDB, ‰)	$^{87}Sr/^{86}Sr$	±σ	Ca (%)	Mg (%)	Mn (ppm)	Rb (ppm)	Sr (ppm)	Mn/Sr	Mg/Ca	$^{85}Rb/^{86}Sr$
XBK-3	Yurtus	phosphorite	4.5			0.708852	0.000008	1.33	0.55	1.50	0.13	578		0.41	0.000917
XBK-4	Yurtus	dolostone	6.5	-2.63	-6.32	0.709560	0.000007	34.6	17.7	415	2.30	362	1.15	0.51	0.000787
XBK-5	Yurtus	limestone	8.5	-0.58	-12.1					344	0.34	206	1.67		
XBK-6	Yurtus	limestone	9.0	0.46	-13.2	0.708695	0.000011	36.2	0.20	213	0.43	123	1.74	0.01	0.000400
XBK-7	Yurtus	dolostone	9.3	-5.05	-9.20					496	0.35	103	4.84		
XBK-8	Yurtus	dolostone	10.2	-1.90	-7.77	0.709264	0.000009	2.74	0.75	44.9	0.56	63.6	0.70	0.27	0.000506
XBK-9	Yurtus	dolostone	11.0	-0.77	-6.45	0.710168	0.000009	3.27	1.63	121	0.70	24.2	4.98	0.50	0.001347
XBK-10	Yurtus	dolostone	12.0	-1.12	-9.94					950	0.45	68.9	13.8		
XBK-11	Yurtus	dolostone	13.0	-0.05	-8.33					935	0.40	46.9	19.9		
XBK-12	Yurtus	dolostone	13.5	0.30	-8.22					881	0.32	50.2	17.6		
XBK-13	Yurtus	dolostone	14.2	0.73	-7.67	0.709472	0.000009	18.3	10.2	1062	0.37	73.8	14.4	0.56	0.000990
XBK-14	Yurtus	dolostone	15.6	0.61	-6.85					0.10	0.00				
XBK-15	Yurtus	dolostone	17.8	0.30	-7.06					1017	0.34	50.0	20.3		
XBK-16	Yurtus	dolostone	18.7	0.22	-6.99					902	0.33	44.9	20.1		
XBK-17	Yurtus	dolostone	19.5	-0.12	-7.18					966	0.13	43.6	22.1		
XBK-18	Yurtus	dolostone	21.5	-0.53	-7.11					1428	0.34	41.9	34.1		
XBK-19	Yurtus	dolostone	21.5	0.21	-7.53	0.709451	0.000009	18.4	10.8	472	0.43	58.5	8.07	0.59	0.000861
XBK-20	Yurtus	dolostone	21.6	-0.04	-7.73					361	0.08	44.8	8.07		
XBK-21	Xiaoerbrak	dolostone	21.7	0.08	-7.34					277	0.15	53.6	5.16		
XBK-22	Xiaoerbrak	dolostone	24.9	1.21	-7.7	0.708971	0.000009	21.8	12.5	250	0.11	71.7	3.49	0.57	0.000793
XBK-23	Xiaoerbrak	dolostone	25.9	1.26	-7.52					172	0.03	75.9	2.27		
XBK-24	Xiaoerbrak	dolostone	31.6	2.20	-6.79	0.708817	0.000011	23.8	13.9	136		91.4	1.49	0.58	0.000392
XBK-25	Xiaoerbrak	dolostone	33.4	2.54	-7.05					147		89.2	1.65		
XBK-26	Xiaoerbrak	dolostone	36.1	1.73	-7.39					129		67.4	1.92		
XBK-27	Xiaoerbrak	dolostone	41.4	2.78	-7.26	0.708790	0.000009	19.0	11.3	142		81.7	1.73	0.59	0.001545
XBK-28	Xiaoerbrak	dolostone	45.9	2.59	-6.71					139		92.2	1.51		

Sample	Formation	Lithology	Height (m)	$\delta^{13}C$ (V-PDB, ‰)	$\delta^{18}O$ (V-PDB, ‰)	$^{87}Sr/^{86}Sr$	±σ	Ca (%)	Mg (%)	Mn (ppm)	Rb (ppm)	Sr (ppm)	Mn/Sr	Mg/Ca	$^{85}Rb/^{86}Sr$
XBK-29	Xiaoerbrak	dolostone	52.4	2.55	-6.97	0.708765	0.000009	21.9	12.9	117		73.7	1.58	0.59	0.000309
XBK-30	Xiaoerbrak	dolostone	59.5	2.69	-7.32					124		67.3	1.84		
XBK-31	Xiaoerbrak	dolostone	63.1	2.99	-7.33	0.708731	0.000009	21.2	12.5	132	0.09	87.7	1.50	0.59	0.000555
XBK-32	Xiaoerbrak	dolostone	63.3	2.89	-7.23					111		73.2	1.51		
XBK-33	Xiaoerbrak	dolostone	65.4	3.18	-7.59					96.0		83.9	1.14		
XBK-34	Xiaoerbrak	dolostone	71.6	3.12	-6.94	0.708733	0.000009	20.8	12.2	122		112	1.08	0.58	0.000373
XBK-35	Xiaoerbrak	dolostone	75.9	3.17	-7.24					101		74.5	1.36		
XBK-36	Xiaoerbrak	dolostone	80.3	2.87	-8.49					112		55.5	2.02		
XBK-37	Xiaoerbrak	dolostone	85.5	2.96	-7.96	0.708803	0.000008	21.4	12.8	124		65.2	1.91	0.59	0.000649
XBK-38	Xiaoerbrak	dolostone	90.3	2.66	-8.78					141		64.4	2.18		
XBK-39	Xiaoerbrak	dolostone	103.7	2.73	-8.27					134		53.9	2.49		
XBK-40	Xiaoerbrak	dolostone	113.7	3.15	-7.12	0.708817	0.000015	20.0	11.8	82.8		45.3	1.83	0.59	0.000562
XBK-41	Xiaoerbrak	dolostone	118.0	2.70	-8.24					109	0.03	43.8	2.48		
XBK-42	Xiaoerbrak	dolostone	123.5	2.47	-7.32	0.708888	0.00001	20.6	11.6	91.1		47.7	1.91	0.56	0.000990
XBK-43	Xiaoerbrak	dolostone	126.5	1.73	-7.21					95.8		36.5	2.62		
XBK-44	Xiaoerbrak	dolostone	132.6	2.07	-6.90	0.708810	0.000009	19.5	11.5	92.5		43	2.15	0.59	0.000599
XBK-45	Xiaoerbrak	dolostone	135.6	2.66	-6.44					72.6		30.9	2.35		
XBK-46	Xiaoerbrak	dolostone	142.6	2.85	-6.41					95.4		35.2	2.71		
XBK-47	Xiaoerbrak	dolostone	145.0	2.86	-6.45	0.708788	0.000009	17.8	10.6	86.7		36.0	2.41	0.60	0.000567
XBK-48	Xiaoerbrak	dolostone	149.4	2.33	-6.81					120		39.8	3.02		
XBK-49	Xiaoerbrak	dolostone	151.6	2.43	-6.44					112		39.5	2.83		
XBK-50	Xiaoerbrak	dolostone	155.5	2.45	-6.49	0.708795	0.000009	20.3	12.0	114		57.5	1.98	0.59	0.000615
XBK-51	Xiaoerbrak	dolostone	159.8	2.46	-6.74					104	0.10	51.9	2.00		
XBK-52	Xiaoerbrak	dolostone	165.3	2.51	-6.45					116	0.06	64.1	1.82		
XBK-53	Xiaoerbrak	dolostone	166.0	2.54	-5.50	0.708831	0.000008	19.7	11.5	98.9	0.11	67.0	1.48	0.59	0.00033
XBK-54	Xiaoerbrak	dolostone	167.5	2.42	-5.60					88.4	0.02	64.6	1.37		

Sample	Formation	Lithology	Height (m)	$\delta^{13}C$ (V-PDB, ‰)	$\delta^{18}O$ (V-PDB, ‰)	$^{87}Sr/^{86}Sr$	±σ	Ca (%)	Mg (%)	Mn (ppm)	Rb (ppm)	Sr (ppm)	Mn/Sr	Mg/Ca	$^{85}Rb/^{86}Sr$
XBK-55	Xiaoerbrak	dolostone	168.9	2.50	-5.61	0.708827	0.00001	5.53	3.01	14.8		24.7	0.60	0.54	0.000830
XBK-56	Xiaoerbrak	dolostone	170.1	2.25	-3.53	0.708796	0.000008	17.3	10.1	79.3	0.12	86.1	0.92	0.58	0.000534
XBK-57	Xiaoerbrak	dolostone	171.7	1.22	-4.56					111	0.09	91.5	1.21		
XBK-58	Xiaoerbrak	dolostone	174.1	0.71	-6.7	0.708962	0.000009	18.8	10.7	135	0.01	62.2	2.17	0.57	0.000761
XBK-59	Xiaoerbrak	dolostone	174.0	1.08	-6.12					139	0.00	60.4	2.31		
XBK-60	Xiaoerbrak	dolostone	176.8	-0.69	-6.33	0.708989	0.000008	17.9	10.3	137	0.14	69.0	1.99	0.58	0.000492
XBK-61	Xiaoerbrak	dolostone	178.2	0.19	-8.09					157	0.32	112	1.40		
XBK-62	Xiaoerbrak	dolostone	179.0	-0.19	-6.05	0.708990	0.000008	19.9	11.3	120	0.04	66.1	1.81	0.57	0.000509
XBK-63	Xiaoerbrak	dolostone	182.3	0.33	-6.08					151	0.19	81.9	1.84		
XBK-64	Xiaoerbrak	dolostone	186.7	0.34	-6.12	0.709057	0.00001	19.3	11.1	110	0.14	77.8	1.41	0.58	0.000517
XBK-65	Xiaoerbrak	dolostone	188.9	-0.14	-6.36					143	0.14	68.7	2.09		
XBK-66	Xiaoerbrak	dolostone	192.5	0.62	-6.10	0.708863	0.00001	18.5	10.4	139	0.03	89.6	1.55	0.56	0.000506
XBK-67	Wusonger	dolostone	196.1	-1.05	-6.47					241	0.19	72.3	3.34		
XBK-68	Wusonger	dolostone	202.5	-1.77	-5.80					323	1.73	106	3.04		
XBK-69	Wusonger	dolostone	210.1	-1.21	-6.44	0.708902	0.000007	16.8	9.45	260	0.21	81.9	3.17	0.56	0.000587
XBK-70	Wusonger	dolostone	213.2	-1.89	-6.33					214	0.94	77.9	2.75		
XBK-71	Wusonger	dolostone	244.7	-1.71	-5.14	0.708934	0.000008	13.5	7.88	207	1.17	97.9	2.11	0.58	0.000747
XBK-72	Wusonger	dolostone	254.7	-1.11	-5.47	0.708980	0.000007	19.1	10.9	273	1.36	209	1.30	0.57	0.000628
XBK-73	Wusonger	dolostone	256.2	-0.21	-5.54	0.708941	0.000007	19.8	10.8	298	0.95	219	1.36	0.55	0.000425
XBK-74	Wusonger	dolostone	257.7	-0.27	-5.76	0.708974	0.000007	20.4	11.8	243	0.92	257	0.94	0.58	0.000378
XBK-75	Wusonger	dolostone	259.2	-0.54	-5.84	0.709179	0.000008	18.1	10.2	335	1.26	203	1.65	0.56	0.000242
XBK-76	Wusonger	dolostone	260.7	-0.31	-5.67	0.709054	0.000008	19.3	10.4	295	1.19	220	1.34	0.54	0.000378
XBK-77	Wusonger	dolostone	262.2	0.98	-5.27	0.709169	0.000009	18.5	10.8	276	0.99	213	1.29	0.58	0.000508
XBK-78	Wusonger	dolostone	263.7	-6.66	-12.9	0.709150	0.000006	2.32	0.15	57.9	3.50	1213	0.05	0.06	0.000209
XBK-79	Wusonger	dolostone	265.2	-0.67	-5.59					314	1.13	343	0.92		
XBK-80	Wusonger	dolostone	266.7	-1.18	-5.80					276	0.96	240	1.15		

Sample	Formation	Lithology	Height (m)	$\delta^{13}C$ (V-PDB, ‰)	$\delta^{18}O$ (V-PDB, ‰)	$^{87}Sr/^{86}Sr$	±σ	Ca (%)	Mg (%)	Mn (ppm)	Rb (ppm)	Sr (ppm)	Mn/Sr	Mg/Ca	$^{85}Rb/^{86}Sr$
XBK-81	Wusonger	dolostone	268.2	-3.65	-5.48	0.708749	0.000008	20.0	11.4	265	0.74	209	1.27	0.57	0.000483
XBK-82	Wusonger	dolostone	269.7	-2.23	-5.77					281	1.16	214	1.31		
XBK-83	Wusonger	dolostone	271.2	-11.7	-5.48	0.708771	0.000008	18.8	10.6	352	0.89	248	1.42	0.56	0.000609
XBK-84	Shayilik	dolostone	273.0	-13.3	-7.75					471	1.48	184	2.56		
XBK-85	Shayilik	dolostone	277.9	-2.60	-6.17	0.708923	0.000009	20.3	9.50	320	0.96	213	1.50	0.47	0.001105
XBK-86	Shayilik	dolostone	285.6	-2.45	-4.81			13.6	7.90	196	2.70	153	1.28	0.58	
XBK-87	Shayilik	dolostone	301.7	-2.44	-6.37	0.708723	0.000008	13.6	7.80	287	1.80	128	2.24	0.57	0.000928
XBK-88	Shayilik	dolostone	308.7	-1.35	-6.98					614	2.52	131	4.68		
XBK-89	Shayilik	limestone	326.2	-0.35	-10.5	0.709021	0.000009	35.3	0.40	330	0.99	615	0.54	0.01	0.000329
XBK-90	Shayilik	limestone	336.4	-0.65	-8.05					217	0.64	201	1.08		
XBK-91	Shayilik	limestone	340.0	-0.08	-8.13	0.708853	0.000010	30.2	3.40	192	0.52	570	0.34	0.11	0.000260
XBK-92	Shayilik	limestone	350.4	-0.61	-8.47					369	0.81	425	0.87		
XBK-93	Awatagh	limestone	369.1	0.67	-5.94					598	3.16	130	4.60		
XBK-94	Awatagh	limestone	371.1	0.97	-8.59	0.708880	0.000007	36.3	0.50	135	0.61	5906	0.02	0.01	0.000746
XBK-95	Awatagh	dolostone	386.0	-0.66	-5.76	0.708892	0.000007	12.0	6.80	484	2.14	144	3.37	0.56	0.000542
XBK-96	Awatagh	dolostone	421.5	0.16	-8.81	0.708988	0.000007	19.2	6.50	1085	0.69	183	5.93	0.34	0.000628
XBK-97	Awatagh	dolostone	449.4	-1.50	-7.03					1109	1.21	180	6.17		
XBK-98	Awatagh	dolostone	449.6	-0.25	-6.47	0.709189	0.000008	15.2	7.10	545	0.70	287	1.90	0.47	0.000849
XBK-99	Awatagh	dolostone	468.1	-0.54	-7.47					82.1	0.55	38.9	2.11		
XBK-100	Awatagh	dolostone	483.0	0.70	-6.31	0.709083	0.000009	11.6	6.20	493	4.76	222	2.22	0.53	0.000347
XBK-101	Awatagh	dolostone	483.0	1.11	-6.82					482	1.15	182	2.65		
XBK-102	Awatagh	dolostone	485.0	1.34	-6.45					284	1.05	268	1.06		
XBK-103	Awatagh	dolostone	498.9	-1.38	-7.07	0.709053	0.000007	14.8	8.20	169	1.31	157	1.07	0.56	0.000289
XBK-104	Awatagh	dolostone	500.2	0.06	-6.94					223	1.56	95.5	2.33		
XBK-105	Awatagh	dolostone	517.6	0.09	-6.63	0.709134	0.000008	17.2	9.60	239	1.30	112	2.14	0.56	0.000610
XBK-106	Awatagh	dolostone	519.0	-1.56	-8.69					159	0.80	81.9	1.94		

Sample	Formation	Lithology	Height (m)	$\delta^{13}C$ (V-PDB, ‰)	$\delta^{18}O$ (V-PDB, ‰)	$^{87}Sr/^{86}Sr$	±σ	Ca (%)	Mg (%)	Mn (ppm)	Rb (ppm)	Sr (ppm)	Mn/Sr	Mg/Ca	$^{85}Rb/^{86}Sr$
XBK-107	Awatagh	dolostone	521.2	-0.58	-6.61					249	1.16	183	1.36		
XBK-108	Xiaquilitagh	dolostone	557.6	-0.41	-6.37	0.709156	0.000011	19.2	11.0	106	0.82	119	0.88	0.57	0.000381
XBK-109	Xiaquilitagh	dolostone	563.9	-0.05	-7.22					149	0.76	106	1.40		
XBK-110	Xiaquilitagh	dolostone	570.8	-0.08	-7.38					105	0.69	76.2	1.38		
XBK-111	Xiaquilitagh	dolostone	594.8	-1.30	-5.04	0.708608	0.000008	19.8	11.2	96.7	0.76	91.3	1.06	0.57	0.000679
XBK-112	Xiaquilitagh	dolostone	603.7	-1.37	-4.43					104	1.12	90.7	1.14		
XBK-113	Xiaquilitagh	dolostone	612.7	-0.96	-6.23	0.709018	0.000008	19.1	10.9	68.2	0.67	116	0.59	0.57	0.000277
XBK-114	Xiaquilitagh	dolostone	615.1	-1.22	-6.50					83	0.64	141	0.59		
XBK-115	Xiaquilitagh	dolostone	623.7	-1.12	-6.32	0.709107	0.000009	20.4	9.80	84.3	1.08	126	0.67	0.48	0.000181
XBK-116	Xiaquilitagh	dolostone	631.9	-1.08	-6.25					64.5	0.74	140	0.46		
XBK-117	Xiaquilitagh	dolostone	643.7	-1.16	-6.10	0.709114	0.000008	19.2	10.7	57.5	0.69	118	0.49	0.56	0.000546
XBK-118	Xiaquilitagh	dolostone	669.2	-0.99	-6.16					65.1	0.79	115	0.57		
XBK-119	Xiaquilitagh	dolostone	694.3	-0.87	-6.55	0.709087	0.000008	15.1	8.10	73.5	0.55	100	0.73	0.54	0.000312
XBK-120	Xiaquilitagh	dolostone	700.8	-1.04	-6.16					88.9	0.72	130	0.69		
XBK-121	Xiaquilitagh	dolostone	712.9	-0.91	-6.37	0.709127	0.000008	16.5	9.00	55.1	0.71	151	0.36	0.54	0.000257
XBK-122	Xiaquilitagh	dolostone	722.6	-1.18	-6.70					59.3	1.10	146	0.41		
XBK-123	Xiaquilitagh	dolostone	738.2	-0.96	-6.37	0.709138	0.000008	18.1	10.0	104	0.80	204	0.51	0.56	0.000450
XBK-124	Xiaquilitagh	dolostone	773.2	-1.17	-6.48					118	0.74	227	0.52		
XBK-125	Xiaquilitagh	dolostone	784.9	-0.97	-6.58	0.709143	0.000009	20.3	11.4	120	0.81	245	0.49	0.56	0.000230
XBK-126	Xiaquilitagh	dolostone	797.9	-0.86	-6.49					69.5	0.77	150	0.46		
XBK-127	Xiaquilitagh	dolostone	816.8	-0.82	-7.17	0.709195	0.000008	21.1	10.4	62.8	0.81	126	0.50	0.49	0.000360
XBK-128	Xiaquilitagh	dolostone	837.0	-0.52	-5.68					73.6	0.77	129	0.57		
XBK-129	Xiaquilitagh	dolostone	870.7	-0.29	-6.03	0.709107	0.000009	18.4	10.1	88.3	0.58	136	0.65	0.55	0.000317

1138

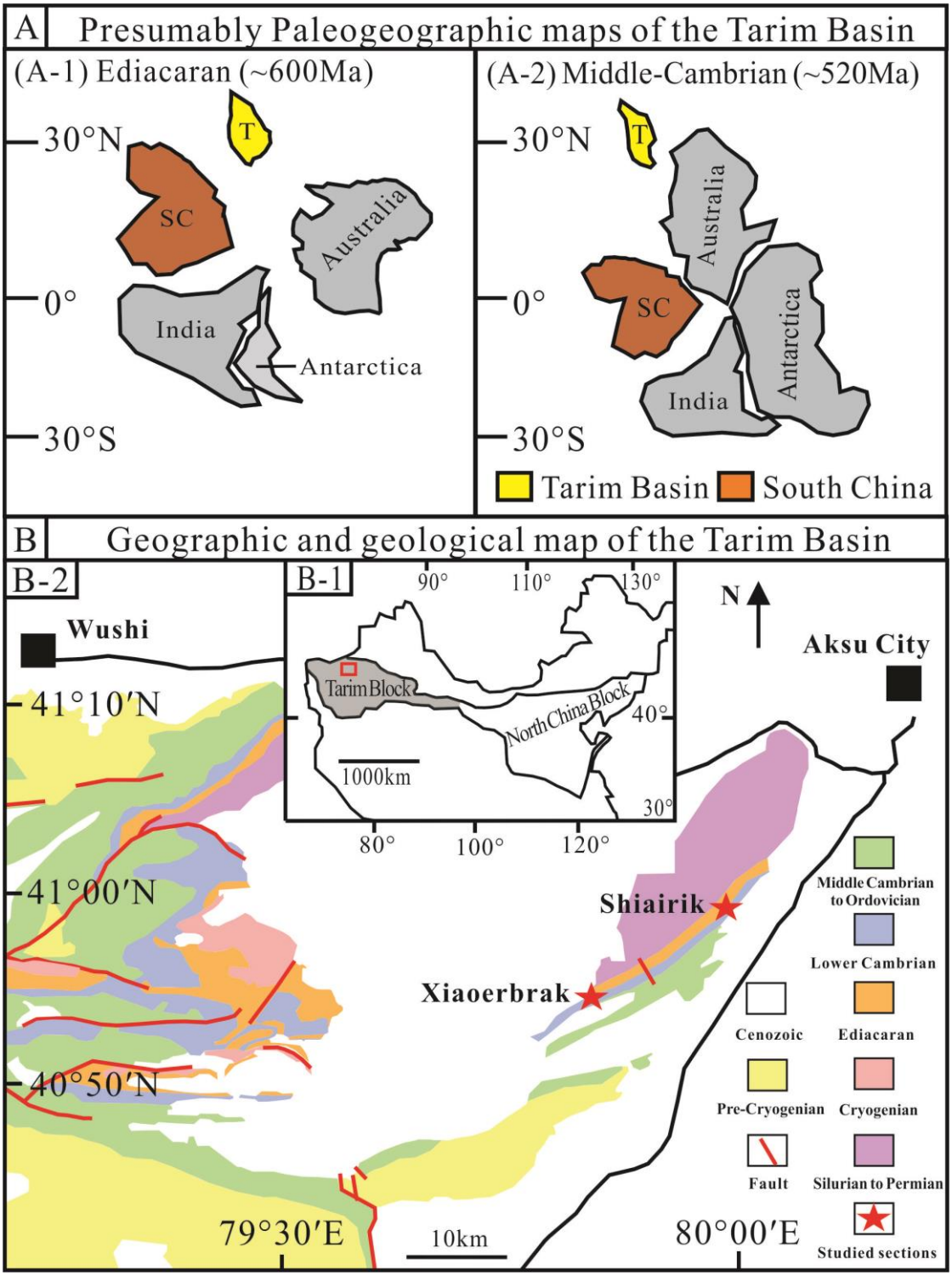
A Presumably Paleogeographic maps of the Tarim Basin
(A-1) Ediacaran (~600Ma)
(A-2) Middle-Cambrian (~520Ma)
30°N
0°
30°S
T
SC
Australia
India
Antarctica
Tarim Basin
South China
B Geographic and geological map of the Tarim Basin
B-2
B-1
Wushi
Aksu City
N
41°10′N
41°00′N
40°50′N
79°30′E
80°00′E
10km
Tarim Block
North China Block
1000km
90°
110°
130°
40°
30°
80°
100°
120°
Shiairik
Xiaoerbrak
Middle Cambrian to Ordovician
Lower Cambrian
Cenozoic
Ediacaran
Pre-Cryogenian
Cryogenian
Fault
Silurian to Permian
Studied sections

Figure 1

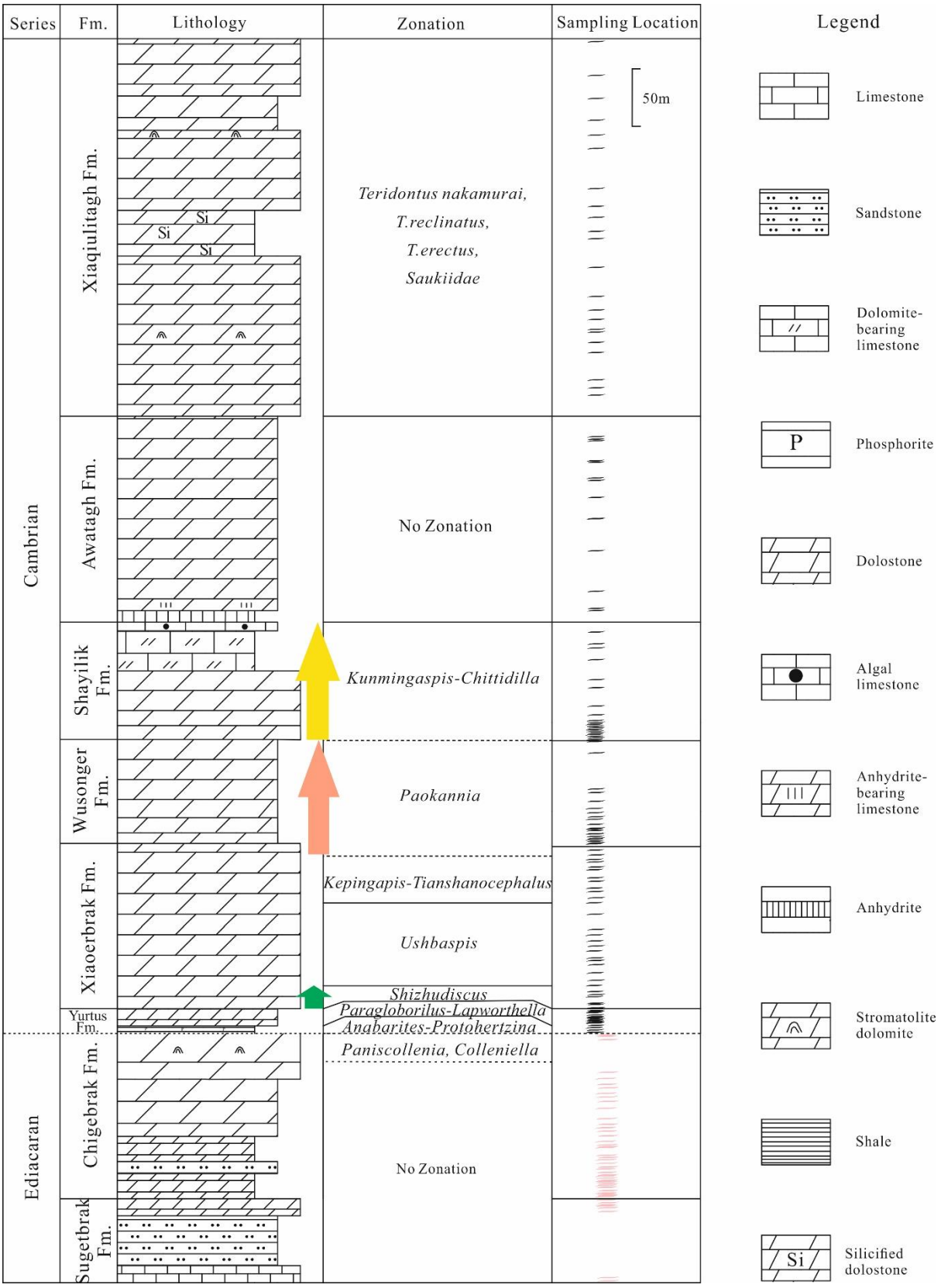
Series
Fm.
Lithology
Zonation
Sampling Location
Legend
Cambrian
Ediacaran
Xiaqiulitagh Fm.
Awatagh Fm.
Shayilik Fm.
Wusonger Fm.
Xiaoerbrak Fm.
Yurtus Fm.
Chigebrak Fm.
Sugetbrak Fm.
Si
50m
Teridontus nakamurai,
T.reclinatus,
T.erectus,
Saukiidae
No Zonation
Kunmingaspis-Chittidilla
Paokannia
Kepingapis-Tianshanocephalus
Ushbaspis
Shizhudiscus
Paragloborilus-Lapworthella
Anabarites-Protohertzina
Paniscollenia, Colleniella
No Zonation
Limestone
Sandstone
Dolomite-bearing limestone
P
Phosphorite
Dolostone
Algal limestone
Anhydrite-bearing limestone
Anhydrite
Stromatolite dolomite
Shale
Si
Silicified dolostone

Figure 2

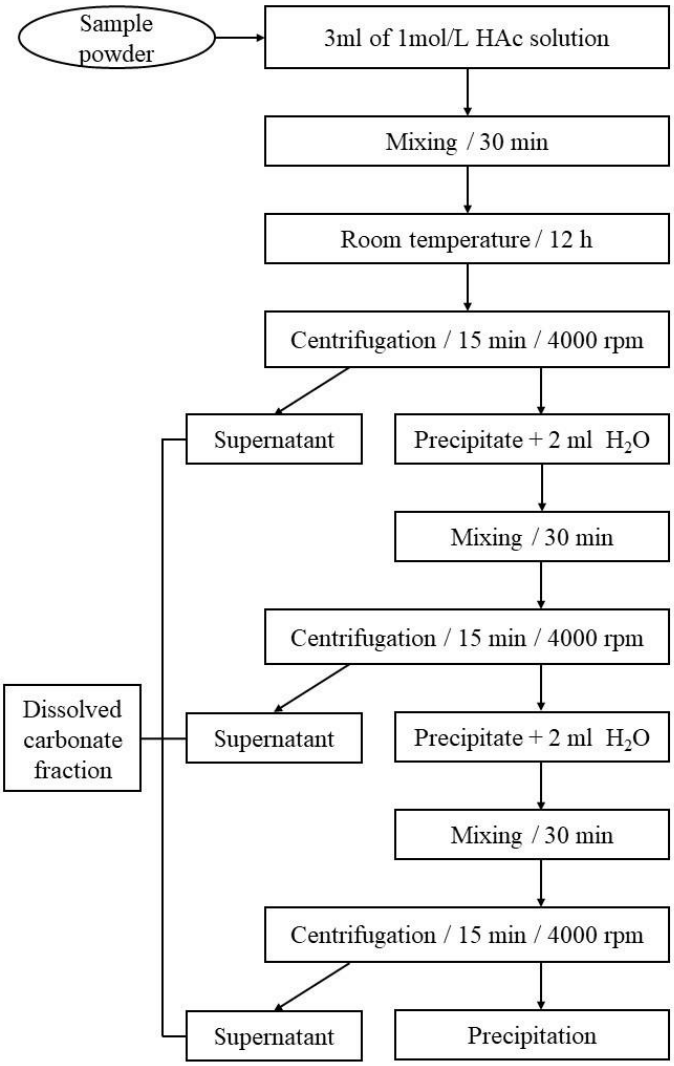

1143

1144 Figure 3

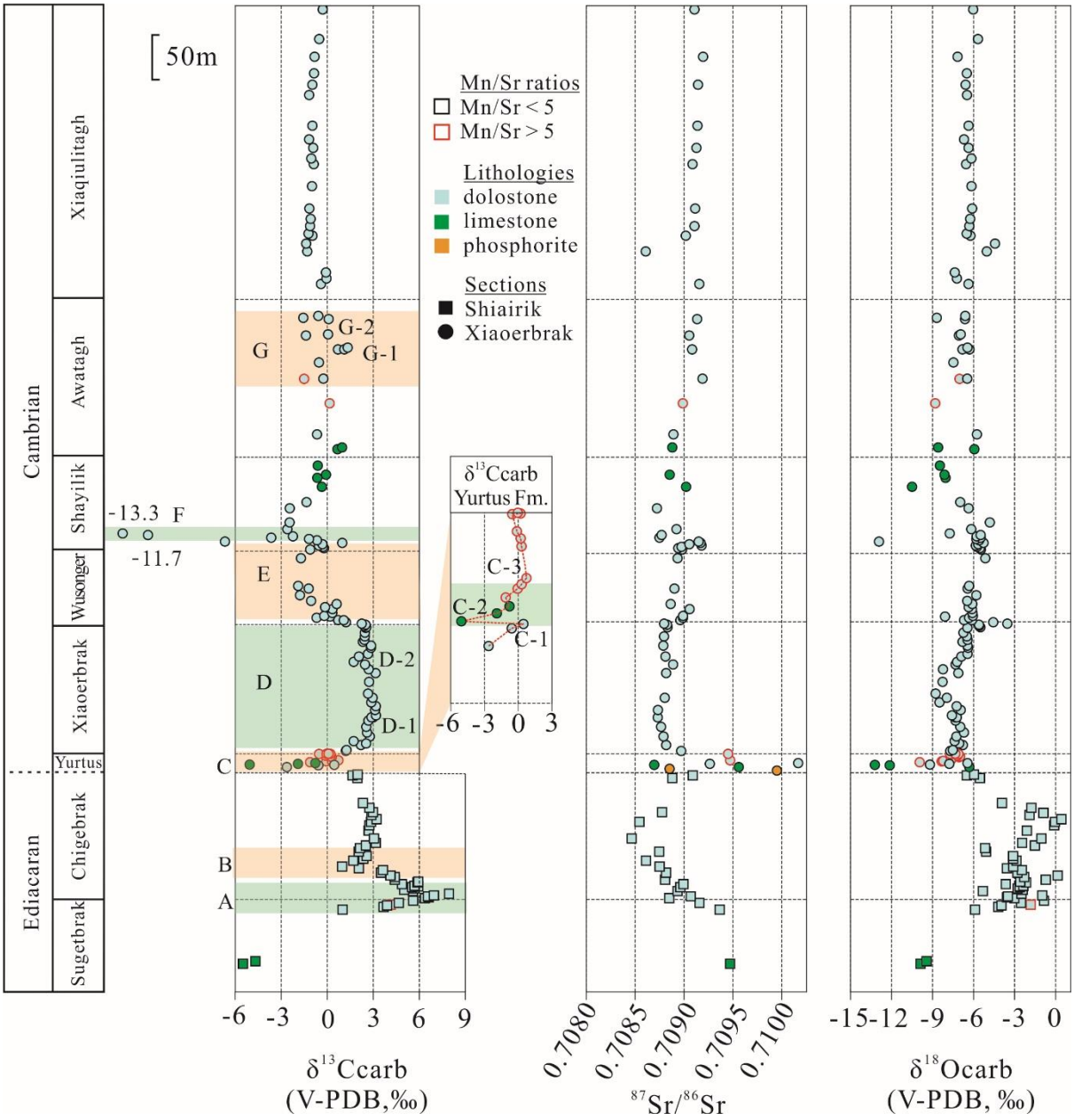
Cambrian
Ediacaran
Xiaqiulitagh
Awatagh
Shayilik
Wusonger
Xiaoerbrak
Yurtus
Chigebrak
Sugetbrak
50m
Mn/Sr ratios
Mn/Sr < 5
Mn/Sr > 5
Lithologies
dolostone
limestone
phosphorite
Sections
Shiairik
Xiaoerbrak
-13.3 F
-11.7
G
G-2
G-1
E
D
D-2
D-1
C
B
A
δ13Ccarb
Yurtus Fm.
C-3
C-2
C-1
-6 -3 0 3
-6 -3 0 3 6 9
δ13Ccarb
(V-PDB,‰)
0.7080 0.7085 0.7090 0.7095 0.7100
87Sr/86Sr
-15-12 -9 -6 -3 0
δ18Ocarb
(V-PDB, ‰)

Figure 4

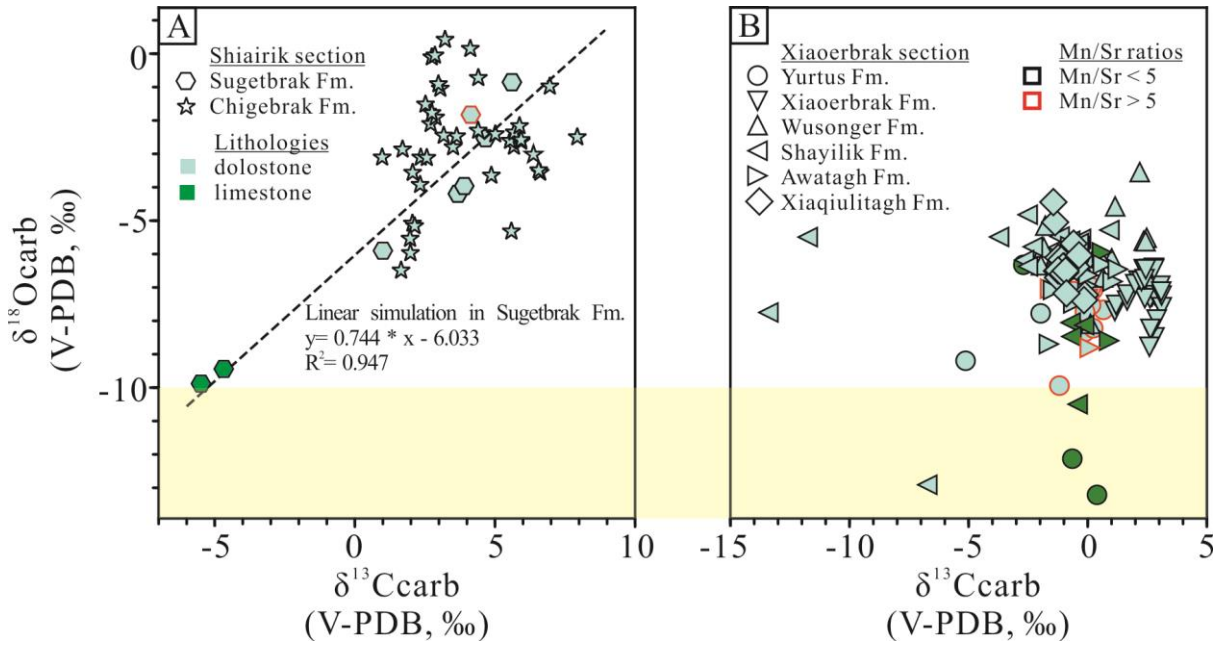

1147

1148 Figure 5

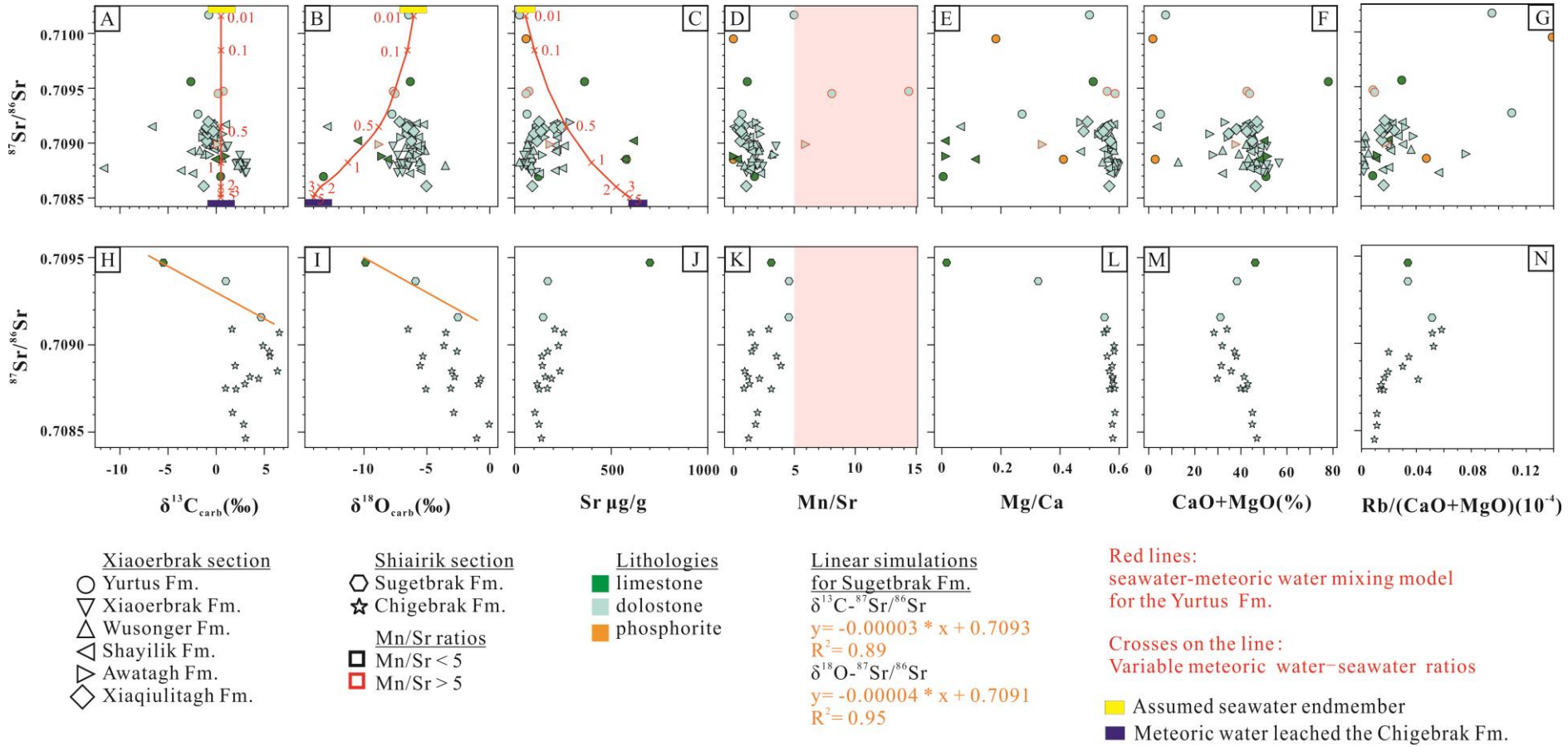
A
B
C
D
E
F
G
H
I
J
K
L
M
N
$^{87}Sr/^{86}Sr$
0.7100
0.7095
0.7090
0.7085
0.01
0.1
0.5
1
2
3
5
$\delta^{13}C_{carb}$(‰)
$\delta^{18}O_{carb}$(‰)
Sr μg/g
Mn/Sr
Mg/Ca
CaO+MgO(%)
Rb/(CaO+MgO)(10^{-4})
Xiaoerbrak section
Yurtus Fm.
Xiaoerbrak Fm.
Wusonger Fm.
Shayilik Fm.
Awatagh Fm.
Xiaqiulitagh Fm.
Shiairik section
Sugetbrak Fm.
Chigebrak Fm.
Mn/Sr ratios
Mn/Sr < 5
Mn/Sr > 5
Lithologies
limestone
dolostone
phosphorite
Linear simulations
for Sugetbrak Fm.
$\delta^{13}C$-$^{87}Sr/^{86}Sr$
y= -0.00003 * x + 0.7093
R^2= 0.89
$\delta^{18}O$-$^{87}Sr/^{86}Sr$
y= -0.00004 * x + 0.7091
R^2= 0.95
Red lines:
seawater-meteoric water mixing model
for the Yurtus Fm.
Crosses on the line:
Variable meteoric water–seawater ratios
Assumed seawater endmember
Meteoric water leached the Chigebrak Fm.

Figure 6

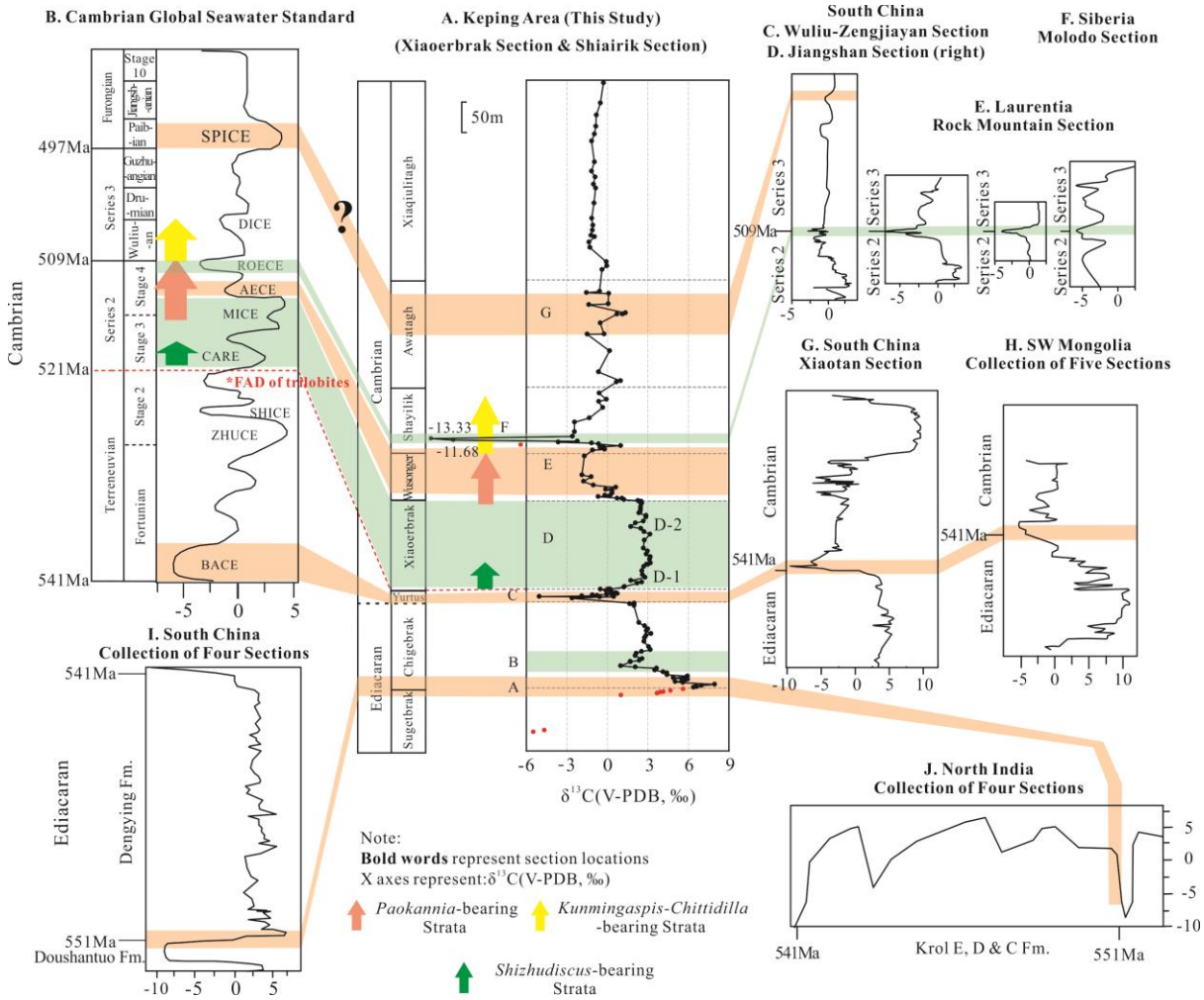
B. Cambrian Global Seawater Standard
A. Keping Area (This Study)
(Xiaoerbrak Section & Shiairik Section)
South China
C. Wuliu-Zengjiayan Section
D. Jiangshan Section (right)
F. Siberia
Molodo Section
E. Laurentia
Rock Mountain Section
G. South China
Xiaotan Section
H. SW Mongolia
Collection of Five Sections
I. South China
Collection of Four Sections
J. North India
Collection of Four Sections
Cambrian
Furongian
Series 3
Series 2
Terreneuvian
Stage 10
Jiangs-hanian
Paib-ian
Guzhu-angian
Dru-mian
Wulu-an
Stage 4
Stage 3
Stage 2
Fortunian
497Ma
509Ma
521Ma
541Ma
SPICE
DICE
ROECE
AECE
MICE
CARE
*FAD of trilobites
SHICE
ZHUCE
BACE
50m
Xiaqiulitagh
Awatagh
Shayilik
Wusongeri
Xiaoerbrak
Yurtus
Chigebrak
Sugetbrak
Ediacaran
G
F
E
D
D-2
D-1
C
B
A
-13.33
-11.68
δ13C(V-PDB, ‰)
Dengying Fm.
551Ma
Doushantuo Fm.
Krol E, D & C Fm.
Note:
Bold words represent section locations
X axes represent:δ13C(V-PDB, ‰)
Paokannia-bearing Strata
Kunmingaspis-Chittidilla -bearing Strata
Shizhudiscus-bearing Strata

Figure 7

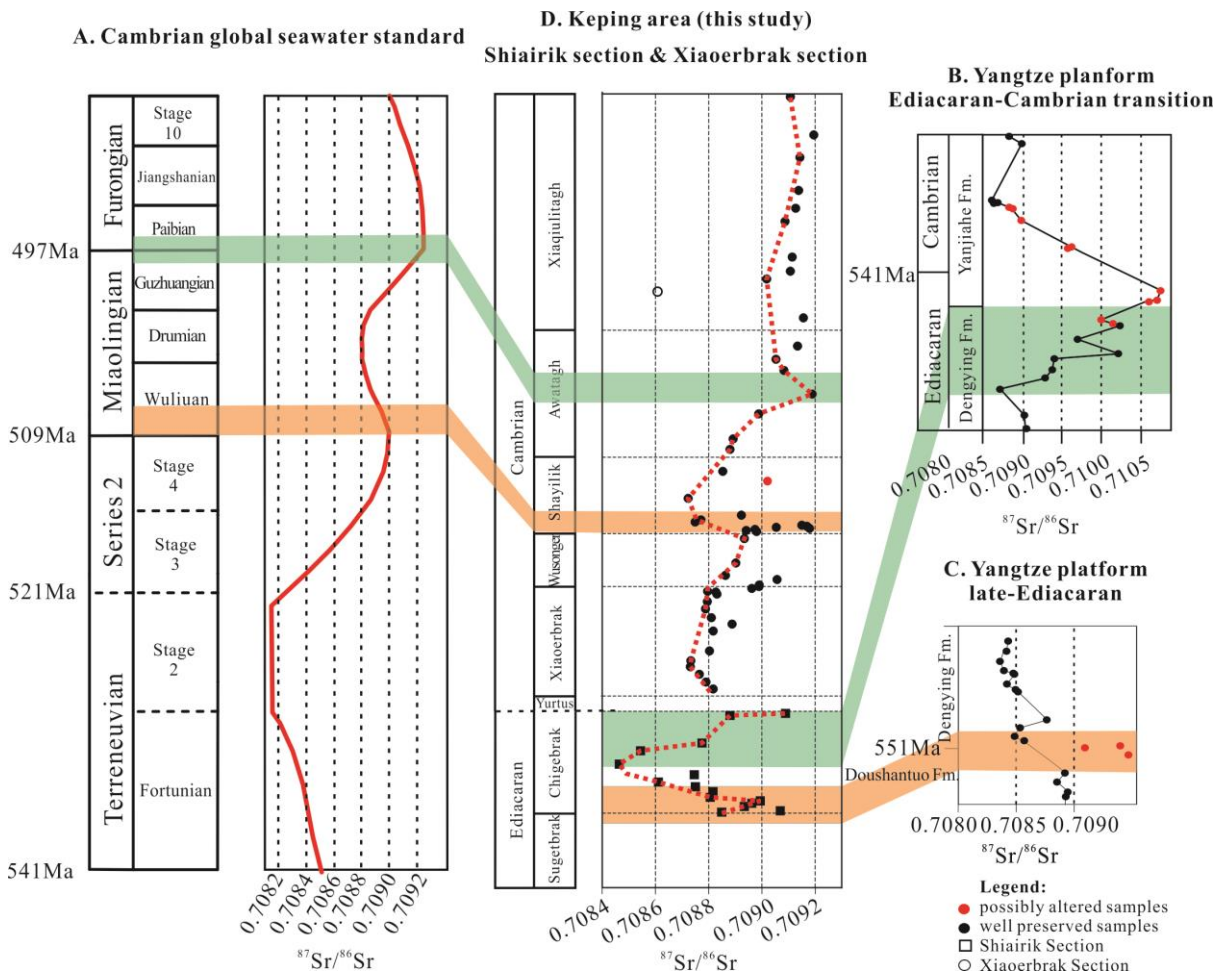
A. Cambrian global seawater standard
D. Keping area (this study)
Shiairik section & Xiaoerbrak section
B. Yangtze planform
Ediacaran-Cambrian transition
C. Yangtze platform
late-Ediacaran
Furongian
Miaolingian
Series 2
Terreneuvian
Stage 10
Jiangshanian
Paibian
Guzhuangian
Drumian
Wuliuan
Stage 4
Stage 3
Stage 2
Fortunian
497Ma
509Ma
521Ma
541Ma
Cambrian
Ediacaran
Xiaqiulitagh
Awatagh
Shayilik
Xiaoerbrak
Yurtus
Chigebrak
Sugetbrak
Yanjiahe Fm.
Dengying Fm.
Doushantuo Fm.
551Ma
0.7080
0.7085
0.7090
0.7095
0.7100
0.7105
0.7082
0.7084
0.7086
0.7088
0.7092
87Sr/86Sr
Legend:
possibly altered samples
well preserved samples
Shiairik Section
Xiaoerbrak Section

Figure 8

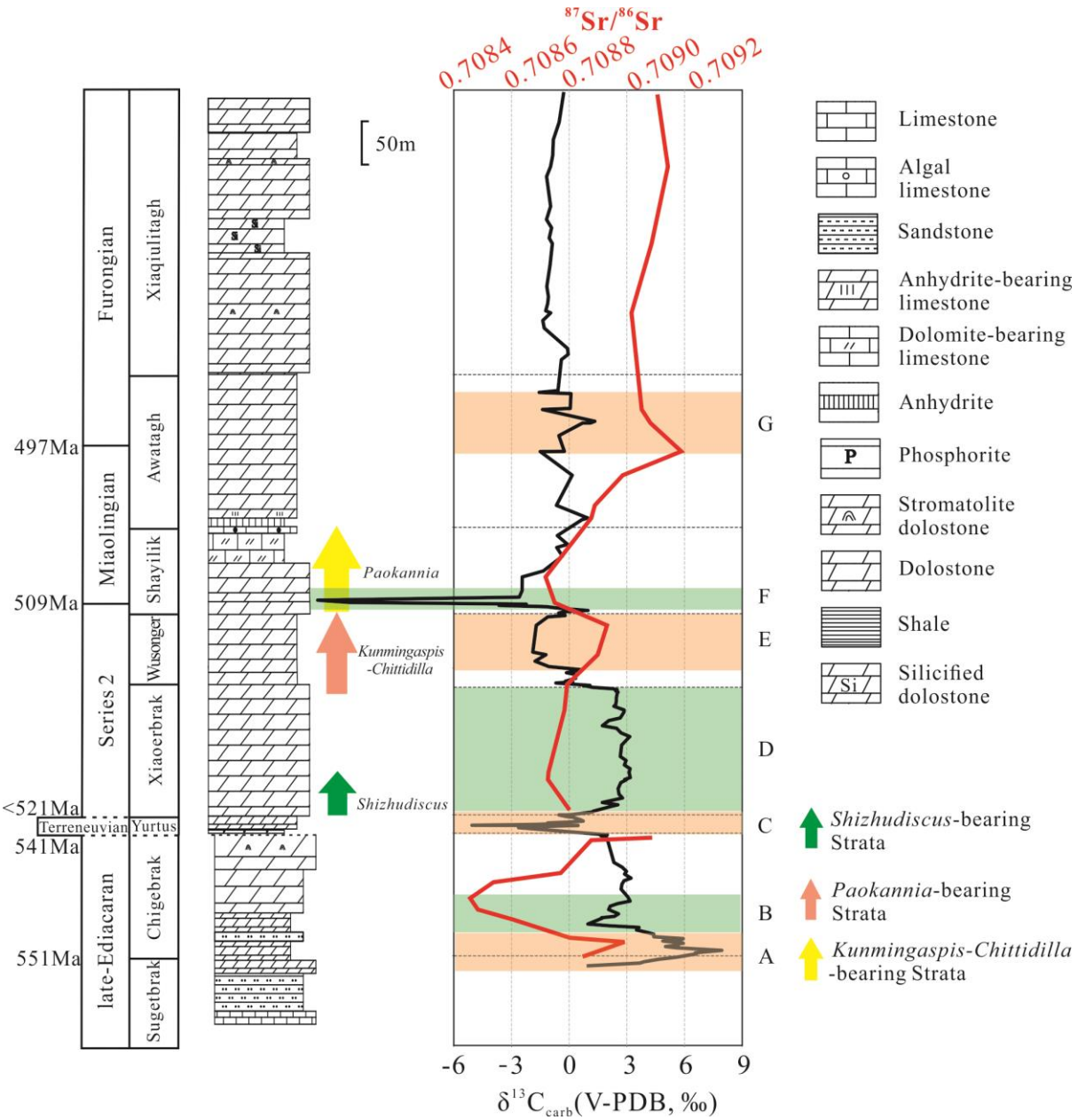
87Sr/86Sr
0.7084
0.7086
0.7088
0.7090
0.7092
50m
Furongian
Miaolingian
Series 2
late-Ediacaran
Xiaqiulitagh
Awatagh
Shayilik
Wusonger
Xiaoerbrak
Chigebrak
Sugetbrak
497Ma
509Ma
<521Ma
Terreneuvian
Yurtus
541Ma
551Ma
Paokannia
Kunmingaspis
-Chittidilla
Shizhudiscus
G
F
E
D
C
B
A
-6
-3
0
3
6
9
δ13Ccarb(V-PDB, ‰)
Limestone
Algal limestone
Sandstone
Anhydrite-bearing limestone
Dolomite-bearing limestone
Anhydrite
Phosphorite
Stromatolite dolostone
Dolostone
Shale
Silicified dolostone
Shizhudiscus-bearing Strata
Paokannia-bearing Strata
Kunmingaspis-Chittidilla -bearing Strata

Figure 9